Towards Quantum Teleportation Assisted by Noiseless Linear Optical Amplification

Hao Jeng

A thesis submitted for the degree of
Bachelor of Philosophy (Honours) (Science)
The Australian National University

October, 2016

Declaration

This thesis is an account of research undertaken between February 2016 and October 2016 at The Department of Physics, Faculty of Science, The Australian National University, Canberra, Australia.

Except where acknowledged in the customary manner, the material presented in this thesis is, to the best of my knowledge, original and has not been submitted in whole or part for a degree in any university.

Hao Jeng
October, 2016

Acknowledgements

I would like to thank my principal supervisor Prof. Ping Koy Lam for giving me the opportunity to work on this wonderful project, and for his wisdom and patience in guiding me through.

Thank you, Assad, for the many helpful suggestions on modelling of the teleporter. Your enthusiasm has made our discussions most enjoyable. Thank you, Jiri, for supervising the 1550 lab work. I had a fantastic time in your fantastic lab.

Thank you, Sophie, for sticking with me while I wrestled with the project. Thank you, Mark, for your wise suggestions on the teleporter. Thank you, Jing Yan, for always being kind and supportive. Thank you to the 1064 team for making the student room the most relaxing and yet the most exciting.

A special thank you to Giovanni and Alex, for helping me kick-start experimental optics. Thank you to all the CQC2T members for your kind hospitality.

Thank you, James, for the smooth running of the Honours year. Thank you, Ben and Carl, for your company.

I would like to thank Sophie and Jiri again, for your tireless efforts in reading the thesis, and for your many helpful suggestions on making it better.

Abstract

This thesis has been divided into a theoretical component and an experimental one. The aim of the theoretical component is to investigate postselection processes on optical quadrature teleportation protocols. We wish to know if postselection filters emulating noiseless linear amplification are capable of increasing teleporter fidelities. The aim of the experimental component is to perform optical quadrature squeezing at the telecom wavelength of 1550nm. We wish to build a bowtie optical parametric amplifier aiming at 15dB of squeezing.

We consider application of postselection on the quantum state teleporter and the squeezing gate teleporter. In the state teleporter, analysing the means and covariance of the teleporter circuit reveals entanglement distillation performed by the NLA-emulating filter, which increases the teleporter fidelity with increasing postselection gain.

In the squeezing gate teleporter, degeneracy of the dual-homodyne detection utilised in the squeezing gate will result in extra degrees of freedom in the electronic gains. The usefulness of the NLA-like filter has been found to be restricted in such a case.

In the 1550nm lab, we establish the necessary experimental components for construction of the squeezer. Within the time limit of this project, we have set up a mode-cleaner, a second harmonic generator for pumping the squeezer cavity, and have also aligned the optical parametric amplifier to the fundamental field.

Contents

List of Figures

1 Introduction

Continuous variable quantum communication has been well known to suffer from loss. This has made squeezing experiments difficult to perform, with very few groups achieving more than 10dB of squeezing. Consequently, the ability to boost entanglement levels of quantum systems becomes much coveted.

In this study, we investigate the application of postselection processes in quantum teleportation protocols to increase the entanglement. Postselection in measurement-based protocols represent cost efficient ways of quantum state processing, some of which may otherwise be difficult and expensive to do directly on a physical optical state

Specifically, we consider both the quantum state teleporter and one of its generalisation known as the squeezing gate teleporter. We consider gate teleporters in hope of extending entanglement distilling postselection schemes to the exciting field of continuous variable cluster state computation.

On the other hand, the 1550nm free space squeezer project aims to produce 15dB of quadrature squeezing with a bowtie singly resonant optical parametric amplifier. The low optical loss at the telecom wavelength suggests a potential arena for squeezing experiments.

This thesis has been divided into five sections. Sections 2 and 3 are background information theory and experimental considerations respectively. In section 4, we discuss the design of the squeezer cavity and present elementary results showing our progress towards squeezing.

In sections 5 and 6, we discuss state teleportation and gate teleportation. We will give brief reviews of canonical teleportation protocols before presenting original work on designing postselection schemes for each of the teleporters.

2 Theory Side

2.1 Classical Light

2.1.1 Laser Beams

The classical light field can be described by **Maxwell's equations**

$$\begin{aligned}
\boldsymbol{\nabla} \cdot \mathbf{D} &= \rho \\
\boldsymbol{\nabla} \cdot \mathbf{B} &= 0 \\
\boldsymbol{\nabla} \times \mathbf{E} &= -\frac{\partial \mathbf{B}}{\partial t} \\
\boldsymbol{\nabla} \times \mathbf{H} &= \mathbf{j} + \frac{\partial \mathbf{D}}{\partial t} \\
\mathbf{D} &= \epsilon_0 \mathbf{E} + \mathbf{P} \\
\mathbf{B} &= \mu_0 \mathbf{H} + \mathbf{M}
\end{aligned} \tag{2.1}$$

In free space, there are no charges ($\rho = 0$, $\mathbf{j} = 0$) and no electric polarisation nor magnetisation ($\mathbf{P} = 0$, $\mathbf{M} = 0$). In such a case, both the electric and magnetic field satisfies the **wave equation**

$$\begin{aligned}
\boldsymbol{\nabla}^2 \mathbf{E} - \frac{1}{c^2} \frac{\partial^2 \mathbf{E}}{\partial t^2} &= 0 \\
\boldsymbol{\nabla}^2 \mathbf{B} - \frac{1}{c^2} \frac{\partial^2 \mathbf{B}}{\partial t^2} &= 0
\end{aligned} \tag{2.2}$$

The wave equation could be solved through separation of variables. With an additional *paraxial* assumption, the resulting electromagnetic waves accurately describe the laser field.

In particular, the spatial modes A under the paraxial approximation are described by the **paraxial Helmholtz equation**

$$(\boldsymbol{\nabla}_x^2 + \boldsymbol{\nabla}_y^2) A + 2ik \frac{\partial A}{\partial z} + 2k^2 A = 0 \tag{2.3}$$

The **transverse electromagnetic modes** (TEM_{mn}) form a complete set of solutions to this equation, the lowest of which is TEM_{00} called the **Gaussian beam**. Although the laser may exist in any of these spatial modes, the Gaussian beam is most often used due to maximal symmetry.

The electric field of the Gaussian beam is given by

$$E(\rho, z) = E_0 \hat{e}_x \frac{w_0}{w(z)} \exp\left(\frac{-\rho^2}{w(z)^2}\right) \exp\left(-i\left(kz + k\frac{\rho^2}{2R(z)} - \psi(z)\right)\right) \tag{2.4}$$

with $\rho = \sqrt{x^2 + y^2}$. Note that the polarisation is linear and along x, according to the unit vector $\hat{e}_x$. The following parameters are used in describing the Gaussian beam:

1. **Beam width**:

$$w(z) = w_0\sqrt{1 + (\frac{z}{z_R})^2} \tag{2.5}$$

As a measure of beam size, it is defined as the $1/e^2$ radius[1], with the Rayleigh range $z_R = \pi w_0^2/\lambda$ which describes the rate of divergence. Apart from the dependence on the wavelength λ, both are characterised by a single parameter known as the **waist** ω_0. This is the corresponds to the minimal size of the beam.

2. **Wavefront curvature**:

$$R(z) = z(1 + \left(\frac{z_R}{z}\right)^2)$$

3. **Gouy phase**:

$$\psi(z) = \arctan(\frac{z}{z_R})$$

It is important to note that a Gaussian beam along the optical axis allows for only two degrees of freedom: the **waist size** and **waist position**. This means Gaussian beams are experimentally friendly to work with.

More generally, real laser beams can have elliptical cross-sections instead of perfect cylindrical symmetry. Such beams are modelled by treating the two dimensions independently using different beam widths. Similarly, there exist astigmatic beams for which light rays in the tangential and sagittal planes do not focus at the same spot. This can be modelled by using different waist positions.

In both cases, the Gouy phase can be calculated independently and summed up as a single value.

2.1.2 Quadratures

From the wave equation 2.2, one finds that a monochromatic linearly polarised light has an electric field amplitude of the form

$$E(r,t) = E_0\left(\alpha(r,t)e^{i\omega t} + \overline{\alpha(r,t)}e^{-i\omega t}\right) \tag{2.6}$$

which can also take the form

$$E = 2E_0(x\cos(\omega t) - p\sin(\omega t)) \tag{2.7}$$

with x and p chosen such that $\alpha = x + ip$. In this way, one measures the electric field relative to a reference wave $\cos(\omega t)$, with x measuring the **in-phase** amplitude and p the **out-of-phase** amplitude.

[1]The radius at which the intensity drops to $1/e^2$ of the value on the optical axis.

The in-phase and out-of-phase quadratures x and p are also known as the **amplitude** and **phase** quadratures, respectively.[2]

2.2 Quantising Light

2.2.1 Canonical Quantisation

Similar to the wave equations for the electric and magnetic fields, one also has a wave equation for the **vector potential** $A(r,t)$ in the Coulomb gauge[2]

$$\boldsymbol{\nabla}^2 A - \frac{1}{c^2}\frac{\partial^2 A}{\partial t^2} = 0 \tag{2.8}$$

Denoting the positive and negative frequency parts of A by A^+ and A^-, one has

$$A^-(r,t) = \frac{1}{\sqrt{2\pi}}\int_{-\infty}^{0} d\omega\ \mathcal{A}(r,\omega)e^{-i\omega t} \tag{2.9}$$

$$A^+(r,t) = \frac{1}{\sqrt{2\pi}}\int_{0}^{\infty} d\omega\ \mathcal{A}(r,\omega)e^{-i\omega t} \tag{2.10}$$

Direct computation shows that they are conjugates

$$\overline{A^-(r,\omega)} = A^+(r,-\omega) \tag{2.11}$$

Hence for simplicity, we can consider the postive frequency part only. An **orthonormal expansion** allows one to write

$$A^+(r,t) = \sum_k c_k u_k(r) e^{-i\omega_k t} \tag{2.12}$$

The u_k's represent different oscillator modes of the electromagnetic field, and are required to satisfy the following four constraints: the free space wave equation, Coulomb gauge condition, orthonormality, and completeness.

The rules of canonical quantisation dictates that these classical oscillator modes become quantum oscillators:

$$\hat{A}(r,t) = \sum_k \left(\frac{\hbar}{2\omega_k \epsilon_0}\right)^{1/2}\left(\hat{a}_k u_k(r)e^{-i\omega_k t} + \hat{a}_k^\dagger \overline{u_k(r)} e^{i\omega_k t}\right) \tag{2.13}$$

Since the electric field is related to the vector potential by

$$E = -\frac{\partial A}{\partial t} \tag{2.14}$$

[2] $\boldsymbol{\nabla}\cdot A = 0$

direct calculation gives

$$\hat{E}(r,t) = i\sum_k \left(\frac{\hbar\omega_k}{2\epsilon_0}\right)^{1/2} \left(\hat{a}_k u_k(r) e^{-i\omega_k t} - \hat{a}_k^\dagger \overline{u_k(r)} e^{i\omega_k t}\right) \tag{2.15}$$

From here, the usual quantum mechanics of canonical quantisation applies. For example, the Hamiltonian of the electromagnetic field is given by

$$\hat{H} = \sum_k \hbar\omega_k \left(\hat{a}_k^\dagger \hat{a}_k + \frac{1}{2}\right) \tag{2.16}$$

2.2.2 Quantised Quadratures

Similar to the classical case, the quadrature observables are defined through the equations [13]

$$\hat{x} = \sqrt{\frac{\hbar}{2\omega}}(\hat{a} + \hat{a}^\dagger) \tag{2.17}$$

$$\hat{p} = \frac{1}{i}\sqrt{\frac{\hbar\omega}{2}}(\hat{a} - \hat{a}^\dagger) \tag{2.18}$$

and the quantised electric field is also similar to the classical case

$$\hat{E} = 2E_0\left(\hat{x}\cos(\omega t) - \hat{p}\sin(\omega t)\right) \tag{2.19}$$

Since the annihilation and creation operators satisfy the relation $[\hat{a}, \hat{a}^\dagger] = 1$, from the defining equations one can derive $[\hat{x}, \hat{p}] = i\hbar$ which shows the non-commutativity of $\hat{x}$ and $\hat{p}$.

The units of $\hbar$ is a matter of taste, and many authors prefer other conventions. The frequency ω is always set to unity.

Throughout this thesis, we will use the convention $\hbar = 1/2$. The annihilation operator thus reads $\hat{a} = \hat{x} + i\hat{p}$, and the Heisenberg uncertainty principle of the x and p quadratures is

$$\Delta\hat{x}^2 \Delta\hat{p}^2 \geq \frac{1}{16} \tag{2.20}$$

Physically, the uncertainty principle of the quadrature observables reflects the uncertainty in simultaneous measurements of the amplitude and phase.

We will reserve the terms *amplitude* and *phase* for the x and p quadratures as they are defined. However, they are not the only sensible definitions of quadratures. In fact, our definition depended on the choice of the reference wave $\cos(\omega t)$, and any phase shift will give rise to an equally valid pair of orthogonal qudratures like x and p.

In such a way, one may express the electric field as a function of these general quadrature observables:

$$\hat{E} = 2E_0\left(\hat{x}^{(\theta)}\cos(\omega t - \theta) - \hat{p}^\theta \sin(\omega t - \theta)\right) \tag{2.21}$$

which are related to the amplitude and phase quadratures by rotations:

$$\begin{bmatrix} \hat{x}^{(\theta)} \\ \hat{p}^{(\theta)} \end{bmatrix} = \begin{bmatrix} \cos\theta & \sin\theta \\ -\sin\theta & \cos\theta \end{bmatrix} \begin{bmatrix} \hat{x} \\ \hat{p} \end{bmatrix} \tag{2.22}$$

It is useful to observe that the quadratures in $\theta \in [\pi, 2\pi)$ are simply those in $\theta \in [0, \pi)$ with the sign changed.

2.3 Graphical Representations

There are many nice graphical techniques for prividing intuition to quantum optical systems. The ones we give here turns out to be simple generalisation of classical methods.

2.3.1 Ball-on-Stick

The classical analogue of the **ball-on-stick** pictures is phase space distributions. The uncertainty principle forbids simultaneous measurements of the amplitude and phase quadratures, thus quantum states of the electromagnetic field cannot be described by a single complex amplitude, but rather by a distribution around the amplitude.

Concretely, ball-on-stick figures are contours of the Wigner function.

2.3.2 Quantum Sidebands

The ball-on-stick picture in the previous section is strictly speaking for a monochromatic field. One can concatenate all of these pictures at different frequencies to form the sideband diagram.[27] As an important example of its applicability, squeezing manifests itself as EPR-like entanglement between upper and lower sidebands in such a picture.

Zero classical amplitude corresponds to a normally distributed phasor with mean zero and variance given by the quantum noise. The phasors at different frequencies are statistically independent of each other.

Mathematically, an arbitrary field in the time domain $\hat{a}(t)$ can be described in the frequency domain through its Fourier transform

$$\hat{a}(\Omega) = \int \hat{a}(t) e^{-i\Omega t}\, dt \tag{2.23}$$

with Ω denoting the sideband frequencies; positive for lower and negative for upper. The creation operator in the frequency domain can be computed through the annihilation operator

$$\hat{a}^\dagger(\Omega) = (\hat{a}(\Omega))^\dagger \tag{2.24}$$

The amplitude and phase quadratures can be defined similarly

$$\hat{x}(\Omega) = \frac{\hat{a}(\Omega) + \hat{a}^\dagger(\Omega)}{2} \tag{2.25}$$

$$\hat{p}(\Omega) = \frac{\hat{a}(\Omega) - \hat{a}^\dagger(\Omega)}{2i} \tag{2.26}$$

and satisfy the commutation relation

$$[\hat{x}(\Omega), \hat{p}(\Omega')] = \frac{i}{2}\delta(\Omega - \Omega') \tag{2.27}$$

Armed with these definitions, one can now describe a signal in terms of the corresponding sidebands generated when mixed with a carrier.

For an arbitrary RF signal expressed in the time domain

$$\hat{x}_{signal}(t) = \frac{1}{2}(\hat{a}(t) + \hat{a}^\dagger(t)) \tag{2.28}$$

$$\hat{p}_{signal}(t) = \frac{1}{2i}(\hat{a}(t) - \hat{a}^\dagger(t)) \tag{2.29}$$

Fourier transformation leads to the frequency domain expressions

$$\begin{aligned} \hat{x}_{signal}(\Omega) &= \frac{1}{2}\left(\hat{x}(\Omega) + \hat{x}(-\Omega) + i(\hat{p}(\Omega) - \hat{p}(-\Omega))\right) \\ \hat{p}_{signal}(\Omega) &= \frac{1}{2}\left(i(-\hat{x}(\Omega) + \hat{x}(-\Omega)) + \hat{p}(\Omega) + \hat{p}(-\Omega)\right) \end{aligned} \tag{2.30}$$

with the sideband dependence made explicit.

2.4 Optical States

Along with quantisation of the electromagnetic field follows the appearance of **quantum noise**. It originates from the Heisenberg uncertainty principle between the amplitude and phase quadrature, therefore requiring more than deterministic field amplitudes in order to describe the quantum states of light.

2.4.1 Coherent States

The **coherent states** are considered to be as classical as quantum states could get. Unlike any other quantum states, these states can be described by a single complex amplitude α, and are denoted by $|\alpha\rangle$.

These also represent the states of an ideal laser beam. Real laser beams suffer from noise, and therefore coherent states are usually produced in the laboratory through modulation.

Mathematically, one could represent the coherent states in the Fock basis by

$$|\alpha\rangle = e^{-|\alpha|^2/2} \sum_{n=0}^{\infty} \frac{\alpha^n}{n!} |n\rangle \tag{2.31}$$

The unitary **displacement operator** $\hat{D}(\alpha)$ is defined as

$$\hat{D}(\alpha) = \exp(\alpha \hat{a}^\dagger - \overline{\alpha}\hat{a}) \tag{2.32}$$

and has the properties

$$\hat{D}(\alpha) |0\rangle = |\alpha\rangle \tag{2.33}$$

$$\hat{D}^\dagger(\alpha) \hat{a} \hat{D}(\alpha) = \hat{a} + \alpha \tag{2.34}$$

which associates it with the creation of coherent states.

The coherent states are also eigenstates of the annihilation operator:

$$\hat{a} |\alpha\rangle = \alpha |\alpha\rangle \tag{2.35}$$

which is the main reason why the annihilation operator can be regarded as the quantised[3] coherent amplitude.

In terms of quadratures, coherent states are **minimal uncertainty states** which saturate the uncertainty principle. Both amplitude and phase quadratures have the same variance of one-quarter, known as the **shot noise limit** (SNL). This value is independent of the coherent amplitude, and so is the same for a vacuum state. It thus represents vacuum noise.

In terms of **photon statistics**, coherent states has a mean photon number equal to the modulus squared of the amplitude

$$\langle \hat{n} \rangle = |\alpha|^2 \tag{2.36}$$

The complete photon number distribution can be calculated directly from its representation in the Fock basis, and is given by a Poissonian distribution

$$|\langle n| \alpha\rangle|^2 = \frac{|\alpha|^{2n}}{n!} \exp(-|\alpha|^2) \tag{2.37}$$

which has the characteristic property for which the variance is numerically equal to the mean.

The family of coherent states form a basis in the Hilbert space of optical states. It turns out that they are **non-orthogonal** and also **overcomplete**. Every coherent state has a nontrivial decomposition in such a basis, viz.

$$|\alpha\rangle = \frac{1}{\pi} \int d\gamma \, |\gamma\rangle \exp(-|\alpha|^2/2 - |\gamma|^2/2 + \alpha\overline{\gamma}) \tag{2.38}$$

[3]The annihilation operator is not Hermitian and therefore strictly speaking not an observable.

However, one retains a convenient form of the **completeness relation** despite the overcompleteness

$$\frac{1}{\pi}\int d\alpha\, |\alpha\rangle\langle\alpha| = \mathbb{1} \tag{2.39}$$

2.4.2 Squeezed States

Coherent states have the same amount of noise[4] as a vacuum state. Squeezed states, on the other hand, are *more quiet* than vacuum. More precisely, one of the quadrature variance can be below the shot noise limit at the expense of a noisy complementary quadrature. In this way, one can beat the vacuum noise level while upholding the Heisenberg uncertainty principle.

Unlike the displacement operator which has a linear Hamiltonian, squeezing operations are described by quadratic Hamiltonians

$$\hat{S}(\zeta) = \exp\left((\overline{\zeta}\hat{a}^2 - \zeta\hat{a}^{\dagger 2})/2\right) \tag{2.40}$$

This operator introduces correlations between upper and lower sidebands, viz.

$$\hat{S}^\dagger(\zeta)\hat{a}\hat{S}(\zeta) = \hat{a}\cosh(r) - \hat{a}^\dagger e^{i\theta}\sinh(r) \tag{2.41}$$

where $\zeta = re^{i\theta}$. This results in **squeezing**, with θ determining the quadrature which is squeezed and r denoting the degree of squeezing. Without loss of generality, choosing $\theta = 0$ gives amplitude squeezing and phase antisqueezing

$$\hat{x} = \hat{S}^\dagger(\zeta)\hat{x}_0\hat{S}(\zeta) = e^{-r}\hat{x}_0 \tag{2.42}$$
$$\hat{p} = \hat{S}^\dagger(\zeta)\hat{p}_0\hat{S}(\zeta) = e^{r}\hat{p}_0 \tag{2.43}$$
$$\tag{2.44}$$

Supposing that $\hat{x}_0 + i\hat{p}_0$ represents a vacuum state, one may calculate the quadrature statistics of $\hat{x} + i\hat{p}$ to be

$$\langle\hat{x}\rangle = \langle\hat{p}\rangle = 0 \tag{2.45}$$
$$\langle\Delta\hat{x}^2\rangle = e^{-2r} < 1 \tag{2.46}$$
$$\langle\Delta\hat{p}^2\rangle = e^{2r} > 1 \tag{2.47}$$

which is a squeezed vacuum state.

[4]In this thesis, we always take the noise to mean *quadrature variance*, and not other fluctuations such as photon numbers.

2.4.3 Thermal States

The minimal uncertainty of coherent states is not always attainable in experiments. **Thermal states** are states which are coherent-like, but with excess noise.

Thermal states are *statistically mixed states*, given by a normal distribution of coherent states

$$\hat{\rho}_{th}(\lambda) = \frac{1}{\pi}\frac{1-\lambda^2}{\lambda^2}\int d\alpha \exp\left(-\frac{1-\lambda^2}{\lambda^2}|\alpha|^2\right)|\alpha\rangle\langle\alpha| \tag{2.48}$$

where λ is a real number between 0 and 1, related to the quadrature variance $\sigma^2 = (1+\lambda^2)/(1-\lambda^2)$.

One can equivalently express this in the Fock basis

$$\hat{\rho}_{th}(\lambda) = (1-\lambda^2)\sum_n \lambda^{2n}|n\rangle\langle n| \tag{2.49}$$

2.4.4 Two Mode Squeezed State

One of the main applications of squeezed states is the construction of quadrature entanglement. Consider amplitude and phase squeezed fields:

$$\hat{x}_1 = e^{+r}\hat{x}_1^{(0)} \tag{2.50}$$
$$\hat{p}_1 = e^{-r}\hat{p}_1^{(0)} \tag{2.51}$$
$$\hat{x}_2 = e^{-r}\hat{x}_2^{(0)} \tag{2.52}$$
$$\hat{p}_2 = e^{+r}\hat{p}_2^{(0)} \tag{2.53}$$

where the (0) superscript denotes vacuum modes. When we combine these two fields at a 50/50 beamsplitter, we obtain:

$$\hat{x}_A = (e^{+r}\hat{x}_1^{(0)} + e^{-r}\hat{x}_2^{(0)})/\sqrt{2} \tag{2.54}$$
$$\hat{p}_A = (e^{-r}\hat{p}_1^{(0)} + e^{+r}\hat{p}_2^{(0)})/\sqrt{2} \tag{2.55}$$
$$\hat{x}_B = (e^{+r}\hat{x}_1^{(0)} - e^{-r}\hat{x}_2^{(0)})/\sqrt{2} \tag{2.56}$$
$$\hat{p}_B = (e^{-r}\hat{p}_1^{(0)} - e^{+r}\hat{p}_2^{(0)})/\sqrt{2} \tag{2.57}$$

One can observe that individual quadratures are very noisy due to the antisqueezing, however the entanglement observables are very quiet

$$\hat{x}_A - \hat{x}_B = \sqrt{2}e^{-r}\hat{x}_2^{(0)} \tag{2.58}$$
$$\hat{p}_A + \hat{p}_B = \sqrt{2}e^{-r}\hat{p}_1^{(0)} \tag{2.59}$$

The quadratures of the output beams from the beamsplitter are *entangled*, and the entanglement increases with increased squeezing.

As the correlations resemble the position and momentum entanglement in the formulation of the Einstein-Podolsky-Rosen paradox, these entangled states are called **EPR beams** whilst been also known as **two-mode squeezed states** (TMSS). These names will be used interchangeably throughout this thesis.

In the Schrödinger picture, we can write the full formula for the TMSS explicitly in the Fock basis:

$$|TMSS\rangle = \sqrt{1-\lambda^2}\sum_{n=0}^{\infty}\lambda^n\,|n,\ n\rangle \tag{2.60}$$

with the entanglement level given by

$$\lambda = \tanh(r) \tag{2.61}$$

which approaches unity as squeezing approaches infinity. In the absence of squeezing, one obtains $\lambda = 0$ corresponding to no entanglement.

Tracing out one beam results in a vacuum thermal state for the other beam, with zero mean coherent amplitude and variance $\langle\Delta\hat{x}^2\rangle = \langle\Delta\hat{p}^2\rangle = 2e^{-2r}$, in agreement with the Heisenberg picture above.

Finally, we record the **covariance matrix** of the two-mode-squeezed state

$$c_{TMSS} = \begin{bmatrix} Cov(\hat{x}_A,\hat{x_A}) & Cov(\hat{x}_A,\hat{p_A}) & Cov(\hat{x}_A,\hat{x_B}) & Cov(\hat{x}_A,\hat{p_B}) \\ Cov(\hat{p}_A,\hat{x_A}) & Cov(\hat{p}_A,\hat{p_A}) & Cov(\hat{p}_A,\hat{x_B}) & Cov(\hat{p}_A,\hat{p_B}) \\ Cov(\hat{x}_B,\hat{x_A}) & Cov(\hat{x}_B,\hat{p_A}) & Cov(\hat{x}_B,\hat{x_B}) & Cov(\hat{x}_B,\hat{p_B}) \\ Cov(\hat{p}_B,\hat{x_A}) & Cov(\hat{p}_B,\hat{p_A}) & Cov(\hat{p}_B,\hat{x_B}) & Cov(\hat{p}_B,\hat{p_B}) \end{bmatrix} \tag{2.62}$$

$$= \frac{1}{4}\begin{bmatrix} \cosh(2r) & 0 & \sinh(2r) & 0 \\ 0 & \cosh(2r) & 0 & -\sinh(2r) \\ \sinh(2r) & 0 & \cosh(2r) & 0 \\ 0 & -\sinh(2r) & 0 & \cosh(2r) \end{bmatrix} \tag{2.63}$$

The covariances of the pairs x_1, x_2 and p_1, p_2 approaches infinity as squeezing r increases, indicating increasing correlations.

2.4.5 Gaussian States

In short, Gaussian states have Wigner functions described by normal distributions. Coherent, squeezed, and thermal states are all Gaussian states; in fact, they are also *the only* such states in the following sense

1. A single mode pure Gaussian state is a displaced squeezed vacuum state $\hat{D}(\alpha)\hat{S}(\zeta)\left|0\right\rangle$

2. A single mode mixed Gaussian state is a displaced squeezed thermal state. $\hat{D}(\alpha)\hat{S}(\zeta)\hat{\rho}_{th}\hat{S}(\zeta)^{\dagger}\hat{D}(\alpha)^{\dagger}$

More generally, one can have multi-mode Gaussian states given by the Wigner function

$$W(x) = \frac{1}{(2\pi)^N\sqrt{\det c}}\exp\left(-\frac{1}{2}(x-\mu)^T c^{-1}(x-\mu)\right) \tag{2.64}$$

The multimode covariance matrix c is required to satisfy the usual properties in probability theory of being real, symmetric, and positive semi-definite. The two-mode-squeezed state is an example of a two mode Gaussian state.

2.5 The Wigner Function

2.5.1 Derivation

Due to the non-commutativity of the amplitude and phase quadratures and hence the quantum noise, distributions in the phase space spanned by x and p become important representations of quantum states. One important example used frequently in this thesis is the **Wigner function**.

The motivation for a Wigner function is the desire of a *probability distribution* in the phase space for quantum states. But such functions cannot satisfy the axioms of probability theory due to the Heisenberg uncertainty principle. Fortunately, it is perfectly fine *marginal distributions* describing only single quadratures to behave as probability distribution. The Wigner function is therefore a **quasiprobability distribution**.

We will take this property as the *defining property* of the Wigner function. It completely determines the formula for the Wigner function.

Concretely, the defining property of the Wigner function is given by

$$\left\langle x^{(\theta)}\right|\hat{\rho}\left|x^{(\theta)}\right\rangle = \int_{-\infty}^{\infty} dp\ W(x\cos\theta - p\sin\theta, x\sin\theta + p\cos\theta) \tag{2.65}$$

On the left hand side is the probability distribution of $\hat{x}^{(\theta)}$. On the right is the marginal distribution corresponding to $\hat{x}^{(\theta)}$. This definition declares that they are equivalent.

With a keen eye, one can identify the right hand side as the **Radon transform** $\mathcal{R}$ of the Wigner function $W(x,p)$

$$\mathcal{R}W(x,\theta) = \int_{-\infty}^{\infty} dp\ W(x\cos\theta - p\sin\theta, x\sin\theta + p\cos\theta) \tag{2.66}$$

The problem therefore reduces to the *inversion* of the Radon transform. To do this, we will link the Radon transform to the Fourier transform and finish it off with a Fourier inversion. The key is the following result on Radon transforms, known in the mathematics community as the **projection-slice theorem**

$$\int \mathcal{R}W(x,\theta)e^{-i\xi x}dx = \hat{W}(\xi\cos\theta, \xi sin\theta) \tag{2.67}$$

where the hat in the equation represents Fourier transform of the Wigner function in both variables. It suffices to simplify this expression and then to invert it. From the defining property one has

$$\hat{W}(\xi cos\theta, \xi\sin\theta) = \int \left\langle x^{(\theta)}\right| \hat{\rho} \left|x^{(\theta)}\right\rangle e^{-i\xi x}\ dx \tag{2.68}$$

Shifting the rotation in $x^{(\theta)}$ onto the exponential gives [18]

$$\hat{W}(u,v) = \int\ dx\ \langle x|\ \hat{\rho}\exp(-i(u\hat{x} + v\hat{p}))\ |x\rangle \tag{2.69}$$

Decomposing the exponential using the Baker-Campbell-Hausdorff formula and then performing Fourier inversion yields an explicit expression for the Wigner function

$$W(x,p) = \frac{1}{2\pi}\int_{-\infty}^{\infty}\ \exp(ipy)\left\langle x - \frac{y}{2}\right| \hat{\rho} \left|x + \frac{y}{2}\right\rangle\ dx \tag{2.70}$$

Note that this expression applies in general to arbitrary operators $\hat{\rho}$, not only to density matrices. Thus we may speak of the Wigner function of observables as well.

2.5.2 Properties

The Wigner behaves like a probability distribution. It is real and normalised. For arbitrary operators $\hat{\mathcal{O}}_1$ and $\hat{\mathcal{O}}_2$, their corresponding Wigner functions satisfy the overlap formula

$$tr(\hat{\mathcal{O}}_1\hat{\mathcal{O}}_2) = 2\pi\int\ dxdp\ W_1(x,p)W_2(x,p) \tag{2.71}$$

Using the overlap formula, the Wigner function can facilitate computations of various quantities such as expectations of observables

$$tr(\hat{\rho}\hat{\mathcal{O}}) = 2\pi\int\ dxdp\ W(x,p)W_{\hat{\mathcal{O}}}(x,p) \tag{2.72}$$

and fidelities (transition probabilities)

$$|\ \langle\phi|\ \psi\rangle\ |^2 = 2\pi\int\ dxdp\ W_\phi(x,p)W_\psi(x,p) \tag{2.73}$$

A peculiar point about Wigner functions is its pointwise boundedness

$$|W(x,p)| \leq \frac{1}{\pi} \tag{2.74}$$

This boundedness originates from the Heisenberg uncertainty principle, which constrains the probability density at any point of the quantum mechanical phase space. More generally, Wigner

functions are allowed to take upon negative values. Thus they do not in general directly represent probability distributions.

Parameters	Description
T_1	input mirror intensity transmission
T_2	output mirror intensity transmission
R_1	input mirror intensity reflection
R_2	output mirror intensity reflection
p	round-trip optical path length
$\exp(\alpha p)$	internal round-trip loss with coefficient α
Properties	
g_m	loss parameter
$g(\nu)$	complex loss parameter
P_{in}	input optical power
P_{out}	output optical power
P_{refl}	reflected optical power
γ	linewidth
FSR	free spectral range
$\mathcal{F}$	finesse

Table 1: Table reproduced from Bachor p122.

3 Experimental Side

3.1 Optical Components

3.1.1 Cavities

Optical cavities form an integral part of the optical circuits which we will consider. As this subject can be found in many textbooks, we only provide a brief summary presenting and explaining the various properties which we shall come across later.

When an incident light field is coupled into the cavity, it will be reflected many times between the two cavity mirrors before getting lost through the output mirror.

For detailed calculations of the intra-cavity interference, see [2]. The result is that the cavity acts like a resonant filter with the following amplitude and phase response in the frequency domain:

$$\frac{P_{out}}{P_{in}} = \frac{T_1 T_2 g(\nu)}{\sqrt{R_1 R_2}|1 - g(\nu)|^2} \tag{3.1}$$

$$\frac{P_{refl}}{P_{in}} = \frac{|R_1 - g(\nu)|^2}{R_1|1 - g(\nu)|^2} \tag{3.2}$$

$$\frac{P_{cav}}{P_{in}} = \frac{T_1}{|1 - g(\nu)|^2} \tag{3.3}$$

$$\phi_{cav} = \arctan\left(\frac{g_m \sin\delta\phi}{1 - g_m \cos\delta\phi}\right) \tag{3.4}$$

$$\phi_{out} = \arctan\left(\frac{-\sin\delta\phi}{g_m - \cos\delta\phi}\right) \tag{3.5}$$

$$\phi_{refl} = \arctan\left(\frac{-T_1\sqrt{R_1}\sin\delta\phi}{\sqrt{R_1} + T_1\sqrt{R_1}(1 - g_m\cos\delta\phi)}\right) \tag{3.6}$$

For a cavity, the **linewidth** is defined to be the full width at half maximum (FWHM) of the resonant peak, and is given by

$$\gamma = \frac{c}{p}(1 - g_m)$$

where g_m denotes the **loss parameter**

$$g_m = \sqrt{R_1 R_2 \exp(\alpha p)}$$

which is the attenuation factor of the field between each round-trip. The **free spectral range (FSR)** is defined by the distance between neighbouring peaks, and is equal to

$$FSR = p/c$$

The **finesse** of the cavity is defined by

$$\mathcal{F} = \frac{FSR}{\gamma} = \frac{\pi\sqrt{g_m}}{1 - g_m}$$

and is analogous to the Q-factor of mechanical and electrical systems. It is the most widely cited quantity for optical cavities.

For a symmetric cavity, the resonance transmission will be 100%. However, for asymmetric cavities there can be reflection of power accompanied by a reduction in resonant transmission. Analogous to the case for electronics, this phenomenon is known as **impedance matching**.

Stable build-up of intra-cavity optical power can only be achieved if the beam does not diverge as it reflects between the mirrors. This results in a non-trivial problem for **optical stability**, with the cavity *optically stable* if and only if[5]

$$0 \leq g_1 g_2 \leq 1$$

where

$$g_k = 1 - \frac{p}{2R_k}$$

The R_k's here denote the radius of curvature of the cavity mirrors. Experimentally, it is always desirable to work *strictly inside* the region of stable configurations.

[5]The stability criterion generalises to ring cavities. [22]

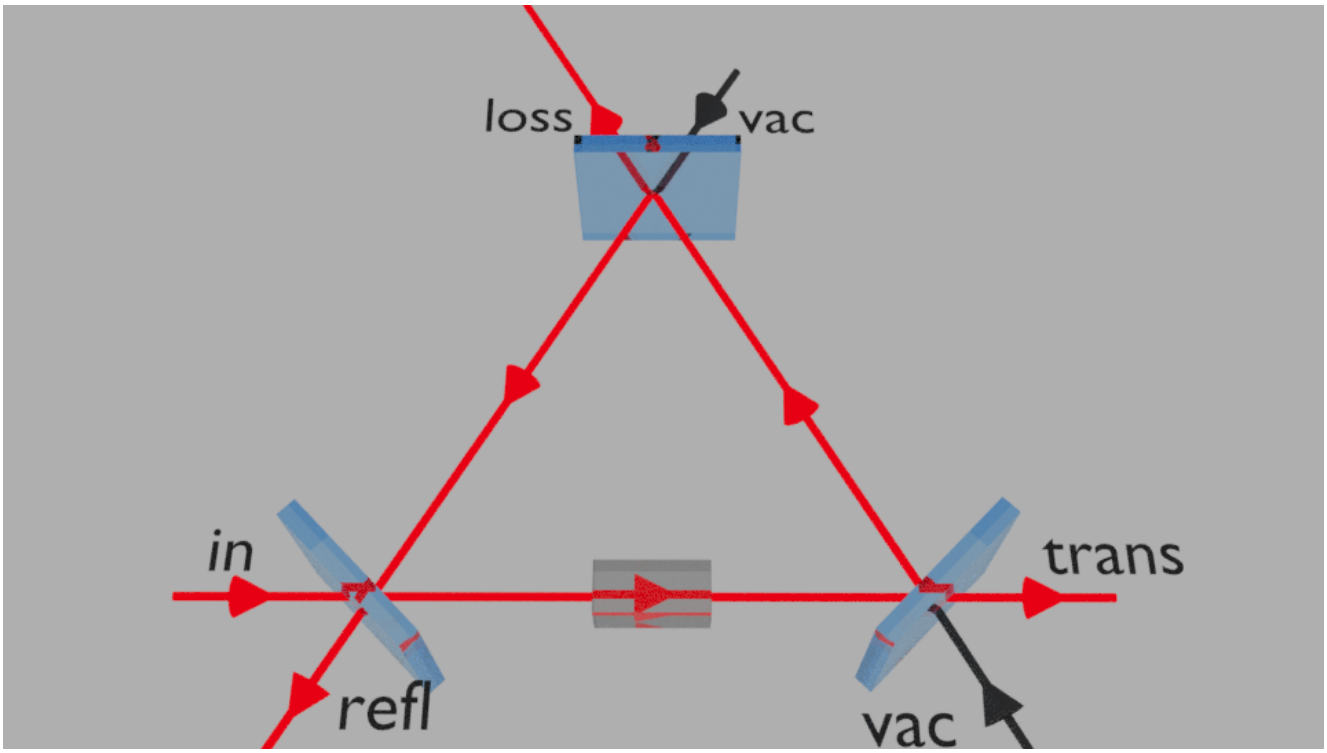

Figure 3.1: Ring cavity with nonlinear crystal.

Given fixed mirror separation and radii of curvature, the cavity supports an unique set of TEM spatial modes. An input light field [6] will therefore be decomposed in this basis, and transmitted (reflected) according to the power and phase response equations. Misalignment will result in higher order modes. By using mirrors and lenses, we can **mode-match** the input beam to the cavity mode. When the input beam is identical to the cavity mode, the coupling into the cavity is maximised and one obtains the ideal case of single peaks.

The higher-order modes resonate at different frequencies. This is due to the **Gouy phase shift**, the value of which depends on the exact mode. Therefore different spatial modes will pick up different phase shifts over the same round-trip, and the resonant frequencies will thus differ. For the special case of confocal cavities, the Gouy phase shift is zero for all spatial modes.

The theory for the linear cavity generalises to ring cavities, and also to the full quantum theory through canonical quantisation. [2]

The general ring cavity is shown in

with any additional mirrors and losses bunched into a single effective mirror between the input and output coupler. This cavity can be described by the quantum Langevin equation

$$\dot{\hat{a}} = -(\kappa - i\Delta)\hat{a} + \sqrt{2\kappa_{in}}\hat{A}_{in} + \sqrt{2\kappa_{out}}\hat{A}_{out} + \sqrt{2\kappa_l}\hat{A}_l \tag{3.7}$$

The detuning Δ can be set to zero when on resonance.

[6] For simplicity, one can assume it is Gaussian.

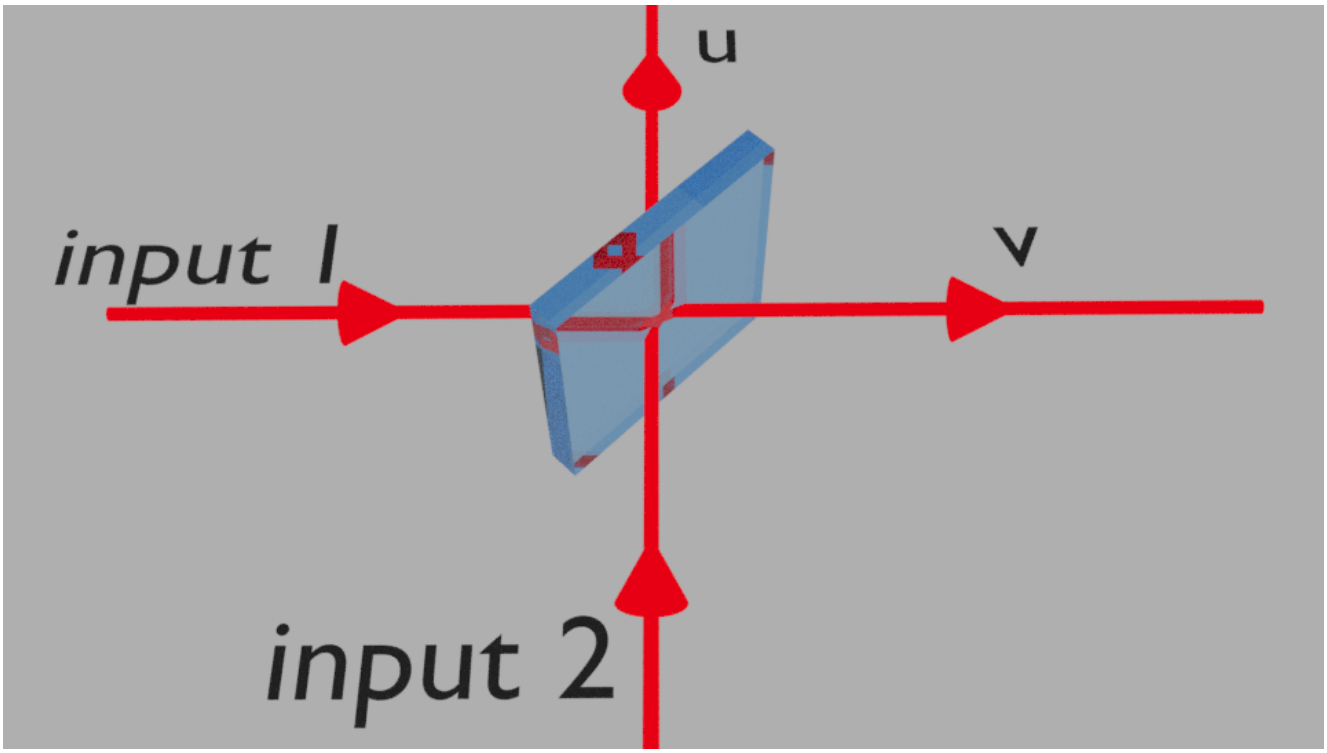

Figure 3.2: Beamsplitter

In the presence of a second order nonlinear material, the cavity equations for the fundamental field $\hat{a}$ and the second harmonic $\hat{b}$ will be given by

$$\begin{aligned}\dot{\hat{a}} &= -(\kappa_a - i\Delta_a)\hat{a} + \epsilon\hat{a}^\dagger\hat{b} + \sqrt{2\kappa_{in}^a}\hat{A}_{in} + \sqrt{2\kappa_{out}^a}\hat{A}_{out} + \sqrt{2\kappa_l^a}\hat{A}_l \\ \dot{\hat{b}} &= -(\kappa_b - i\Delta_b)\hat{b} - \frac{\epsilon}{2}\hat{a}^2 + \sqrt{2\kappa_{in}^b}\hat{B}_{in} + \sqrt{2\kappa_{out}^b}\hat{B}_{out} + \sqrt{2\kappa_l^b}\hat{B}_l\end{aligned} \tag{3.8}$$

which takes into account of the frequency conversion process.

3.1.2 Beam-Splitters

For a lossless beamsplitter with transmission T

the relationship between the input and output fields may be written as

$$\begin{bmatrix} \alpha_u \\ \alpha_v \end{bmatrix} = \begin{bmatrix} \sqrt{T} & -\sqrt{1-T} \\ \sqrt{1-T} & \sqrt{T} \end{bmatrix} \begin{bmatrix} \alpha_1 \\ \alpha_2 \end{bmatrix} \tag{3.9}$$

Note the relative signs: only the field reflected at the low-to-high refractive index interface experienced a π phase shift.

In general, the transmitted fields and reflected fields can experience relative phase shifts distinct from the relation above. It will depend on the exact type of beamsplitter used, but for our purposes the equation above suffices.

In the quantum theory, it suffices to replace the field amplitudes by the annihilation operator:

$$\begin{bmatrix} \hat{a}_u \\ \hat{a}_v \end{bmatrix} = \begin{bmatrix} \sqrt{T} & -\sqrt{1-T} \\ \sqrt{1-T} & \sqrt{T} \end{bmatrix} \begin{bmatrix} \hat{a}_1 \\ \hat{a}_2 \end{bmatrix} \tag{3.10}$$

Note that when one port is a vacuum, the input operator in the equation above for that port is a vacuum mode, and cannot be neglected.

3.1.3 Electro-Optic Modulators

We begin with a review of the classical theory of modulation [9]. It will be useful to consider representations of modulations in both the time and frequency domain.

For amplitude modulation, the signal varies the carrier amplitude to create an envelope. Quantitatively, for a sinusoidal modulation it can be described by

$$V_{AM} = (V_c + V_m \sin \omega_m t) \sin \omega_c t \tag{3.11}$$

with V_c, V_m denoting the carrier and modulation amplitudes, ω_c, ω_m the carrier and modulation frequencies, and v_c the output.

On the other hand, phase modulation is a time varying phase shift. For a sinusoidal variation, it can be described by

$$V_{PM} = V_c \sin(\omega_c t + \Delta\phi \sin \omega_m t) \tag{3.12}$$

with similar notation to amplitude modulation and using $\Delta\phi$ to denote the peak phase deviation.

We can also understand the effect of modulations in the frequency domain. The time domain equations decompose into the frequency components

$$V_{AM} = V_c \sin \omega_c t + \frac{mV_c}{2} (\cos(\omega_c - \omega_m)t - \cos(\omega_c - \omega_m)t)) \tag{3.13}$$

$$V_{PM} = V_c J_0(\Delta\phi) \sin \omega_c t + V_c J_1(\Delta\phi) (\sin(\omega_c + \omega_m)t - \sin(\omega_c - \omega_m)t) + \text{higher order Bessel functions} \tag{3.14}$$

A simple view is that both modulations produce **sidebands** with a difference in frequency to the carrier by the modulation frequency ω_m. Note that the higher-order Bessel functions will quite generally be negligible.

The difference between amplitude and phase modulation lies in the relative phase between the sidebands and the carrier. As the sideband phasors rotate, they cycle through constructive and destructive interference. The constructive interference can occur along the carrier phasor or orthogonal to it. The former results in amplitude modulation while the latter results in phase modulation.

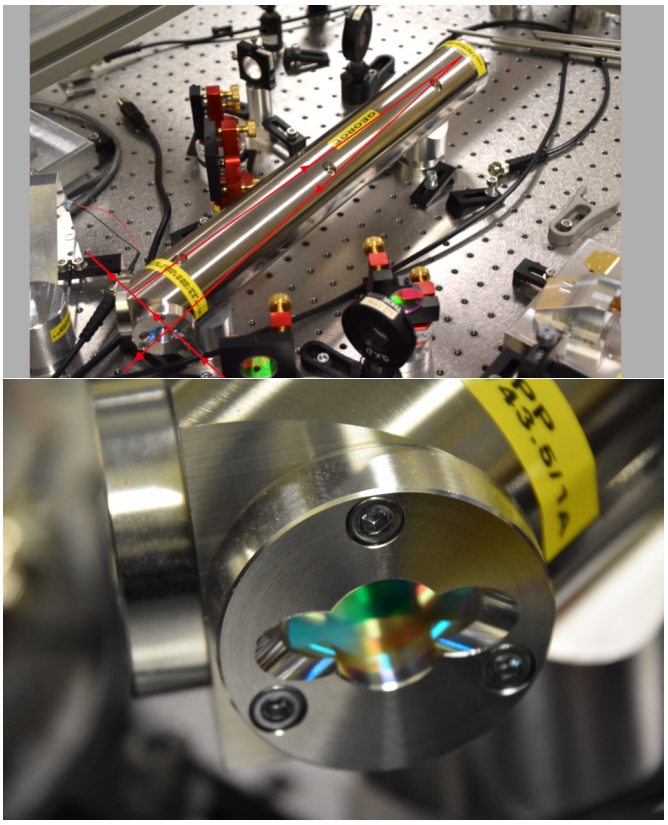

Figure 3.3: Mode cleaner.

The production of amplitude and phase modulations in the optics laboratory relies on the **electro-optic effect**. This requires the use of nonlinear crystals[7] for which the refractive index is dependent on the electric field across the crystal. By applying a electric voltage sinusoidal in time, the variation in the refractive index will induce phase modulation.

The case of amplitude modulation is slightly more involved. The electro-optic effect described above is birefringent, which means that the ordinary and extraordinary axes of the crystal are affected differently by the electric field. Thus a linearly polarised beam entering the crystal at 45° to its axis will experience different phase delays for the different components. Variation in the voltage results in variation in the relative phase, allowing the crystal to act like a variable waveplate and modulate the polarisation state. A linear polariser at the output projects the modulated polarisation onto a single polarisation direction, resulting in amplitude modulation.

3.1.4 Mode Cleaner

To clean the spatial mode of the laser beam and to suppress high frequency laser intensity noise, we use the mode cleaner shown in the photos

This particular mode cleaner has a triangular ring design, with flat input, output mirrors

[7]Commonly lithum niobate ($LiNbO_3$)

optically coupled to a concave back-mirror with radius of curvature of -1000mm. The finesse is about 500.

The mirrors are placed in aluminium caps with an O-ring in between, and screwed onto the body of the mode cleaner directly. Compared to many other versions developed throughout the years (e.g. gluing the mirror onto the mode cleaner body), this design keeps the mirrors clean.

3.2 Photodetection Theory

In the wider physics community, a semiclassical theory (without quantisation of the light field) of photodetection is sufficient. To characterise non-classical states of light, it is necessary to construct a full quantum theoretical description of the process under canonical quantisation. [21]

In this section, we also consider various measurement schemes in quantum optics useful for the characterisation of optical states.

3.2.1 Semiclassical Theory

In order to understand the power of the quantum formalism, one must understand the shortcomings of the semiclassical theory. Below is a brief review of semiclassical photodetection.

In this formalism, one assumes that the incident light can be described by a time-dependent random variable $N(t)$ through an **inhomogeneous Poisson counting process**. This number models the photocount.

Concretely, this means that

1. The photocount begins at zero: $N(0) = 0$
2. The photocount is associated a **rate function** $\lambda(t) = |E(t)|^2$, proportional to the photon number.
3. It has **statistically independent increments**; if $t_1 < t_2 < t_3$ then the increments $N(t_3) - N(t_2)$ and $N(t_2) - N(t_1)$ are independent.
4. Increments are **Poissonian distributed**.

$$Pr(N(t) - N(t_0) = n) = \frac{\left(\int_{t_0}^{t} ds\ \lambda(s)\right)^n}{n!} \exp\left(-\int_{t_0}^{t} ds\ \lambda(s)\right) \tag{3.15}$$

Analysis of the photon statistics results in the following means for the photocount and photocurrent

$$\langle N(t)\rangle = \int_0^t ds\ |E(s)|^2 \tag{3.16}$$

$$\langle i(t)\rangle = q|E(t)|^2 \tag{3.17}$$

consistent with a classical description of photodetection based on the absorption of the light.

However, the covariance function is constrained by

$$\langle \Delta N(t)^2 \rangle \geq \langle N(t) \rangle \tag{3.18}$$

3.2.2 Quantum Theory

The semiclassical theory breaks down in the quantum regime because there exists optical states such as the *squeezed states* which exhibit **sub-Poissonian photon statistics**.

In order to account for these states, it is necessary to formulate photodetection in its quantised form. The translation from semiclassical to quantum photodetection is given below:

The incident light is described by the quantised field $\hat{E}(t)$ given by quantum field theory, with the photocurrent and photocount observables defined by

$$\hat{i}(t) = q\hat{E}^\dagger(t)\hat{E}(t) \tag{3.19}$$

$$\hat{N}(t) = \frac{1}{q}\int_0^t ds\ \hat{i}(s) \tag{3.20}$$

The mean photocount and photocurrent can be obtained by calculating the expectations of the expressions above:

$$\langle \langle N(t) \rangle = \int_0^t ds\ \langle \hat{E}^\dagger(s)\hat{E}(s) \rangle \tag{3.21}$$

$$\langle i(t) \rangle = q\langle \hat{E}^\dagger(t)\hat{E}(t) \rangle \tag{3.22}$$

with the covariance funciton satisfying

$$\langle \Delta \hat{N}(t)^2 \rangle \geq 0 \tag{3.23}$$

Thus quantum theory allows detection of non-classical light with sub-Poissonian photon statistics

$$\langle \Delta \hat{N}^2 \rangle < \langle \hat{N} \rangle \tag{3.24}$$

3.2.3 Homodyne Detection

The setup for the optical homodyne detection is shown in

alongside the well-known electronic homodyne detection. They operate according to the same principles, and thus the optical homodyne is useful for characterising the optical quadratures. We will explain the scheme both quantitatively and the qualitative intuition behind it.

Combination at the beamsplitter of the local oscillator with the input light field is given by

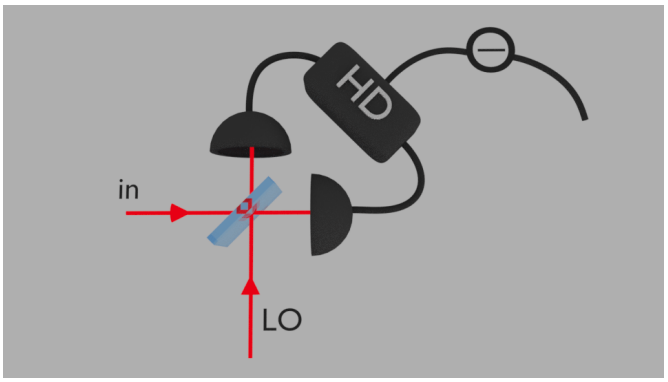

Figure 3.4: Homodyne.

$$\hat{a}_u = \frac{\hat{a}_{LO} + \hat{a}}{\sqrt{2}} \tag{3.25}$$

$$\hat{a}_v = \frac{\hat{a}_{LO} - \hat{a}}{\sqrt{2}} \tag{3.26}$$

In the high-power limit, the local oscillator may be approximated by a single classical amplitude α_{LO}. The light illuminating the two detectors would in such a case be

$$\hat{a}_u = \frac{\alpha_{LO} + \hat{a}}{\sqrt{2}} \tag{3.27}$$

$$\hat{a}_v = \frac{\alpha_{LO} - \hat{a}}{\sqrt{2}} \tag{3.28}$$

The resulting difference current therefore reads

$$\delta\hat{i} = q\hat{a}_u^\dagger \hat{a}_u - q\hat{a}_v^\dagger \hat{a}_v = q(\overline{\alpha_{LO}}\hat{a} + \alpha_{LO}\hat{a}^\dagger) = q|\alpha_{LO}|(\hat{a}e^{-i\theta} + \hat{a}^\dagger e^{i\theta}) \tag{3.29}$$

where θ corresponds to the local oscillator phase. This equation shows us that the difference current can be used to measure any arbitrary quadrature, with quantum noise inclusive.

The quantum model of homodyning is required in order to correctly describe the effect of quantum noise; however, a classical theory suffices to explain the ability of the homodyne detection fore measuring quantum noise.[8]

Using the tools of classical wave optics, one may show that the homodyne detection system is essentially a interferometer:

1. The local oscillator defines a local absolute phase, which can be used to define quadratures.

[8] As a side note, the noise reduction corresponding to squeezing can also be motivated classically. These two examples shows that quantum noise can be considered as *tiny classical fluctuations*, even though its true nature originates from quantum superpositions.

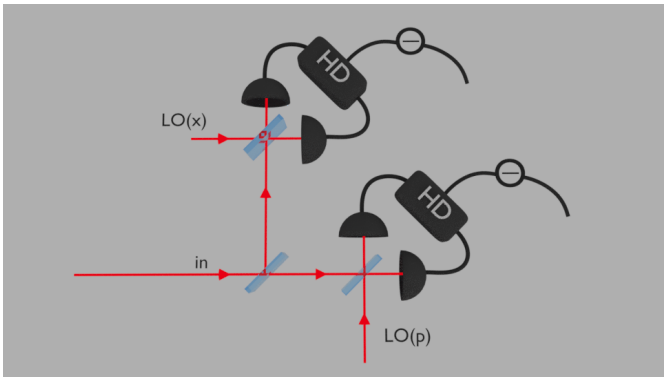

Figure 3.5: Dual homodyne.

2. The in-phase quadrature of the signal will interfere with the LO, but the out-of-phase quadrature will not. The interference term could be thought of as modulation of the local oscillator by the in-phase signal quadrature.

3. The sum current measures the power in the absence of interference, while the difference current measures the interference term and therefore indirectly measures the in-phase signal quadrature.

To conclude, this perspective of homodyning explains the mechanism of measuring signal quadratures and also its associated quantum noise. In particular, the modulation process results in amplification of the signal quadrature by the local oscillator (carrier). The quantum noise is amplified to classically-detectable values through this mechanism.

3.2.4 Heterodyne Detection

Simultaneous measurements of orthogonal quadratures may be performed at the cost of additional noise as dictated by the uncertainty principle. **Heterodyning** is one such example, with the setup given in alertfig. In contrast to homodyning, one employs a frequency shifted local oscillator to interfere with the signal with the resultant field detected by a single photodetector.

Due to the frequency shift, heterodyning turns out to be difficult to perform experimentally.

3.2.5 Dual-Homodyne

There exists an alternative scheme for simultaneous measurements of orthogonal quadratures

The idea is to split-and-measure, and use two homodynes with one measuring the amplitude quadrature and other the phase quadrature.

Similar to heterodyning, we have to pay a price for attempting to measure the amplitude and phase simultaneously. In dual-homodying the price corresponds to the invading vacuum fluctuations from the empty beamsplitter ports.

It turns out that the deal isn't too bad: dual-homodyning is also quantum noise limited. It is usually preferred over heterodyning.

Both heterodyning and dual-homodyning measures the complex amplitude and can be represented in the Schrödinger picture by the coherent projection $\langle\alpha|$ corresponding to an outcome α.

3.3 Experimental Noise and Loss

In this section, we discuss the various sources of inefficiencies in an optical teleporter. However, they are not limited to teleportation alone and occur more generally in most quantum optics experiments.

The experimental inefficiencies which we shall come across can be modelled quantitatively in two ways.

Loss such as nonideal mirrors can be modelled by optical attenuation. *Classical noise* such as the dark noise from photodetectors can be modelled by directly adding a noise operator, with its mean and variance describing the associated classical fluctuations.

3.3.1 Optical Attenuation

Unitary evolutions preserve the commutator between the annihilation and creation operator. Therefore modelling attenuation using the following naïve classical-like transformation fails:

$$\hat{a} \to G\hat{a} \tag{3.30}$$

since

$$[G\hat{a}, G\hat{a}^\dagger] = G^2 \neq [\hat{a}, \hat{a}^\dagger] \tag{3.31}$$

The correct quantum description of optical attenuation is given by [1]

$$\hat{a} \to G\hat{a} + \sqrt{1 - G^2}\hat{\nu} \tag{3.32}$$

Unlike classical theories, stuff can't just dissappear. It will have to be replaced by a vacuum mode $\hat{\nu}$.

A convenient way of thinking about the attenuation is a beamsplitter of transmission G, with the light lost being replaced by invading vacuum noise

3.3.2 Photodiode

The conversion of incoming photons to those which contribute to the photocurrent is not perfect. Semiconductor substrates have photosensitivities dependent on the absorption properties, thickness, wavelength of light, etc.

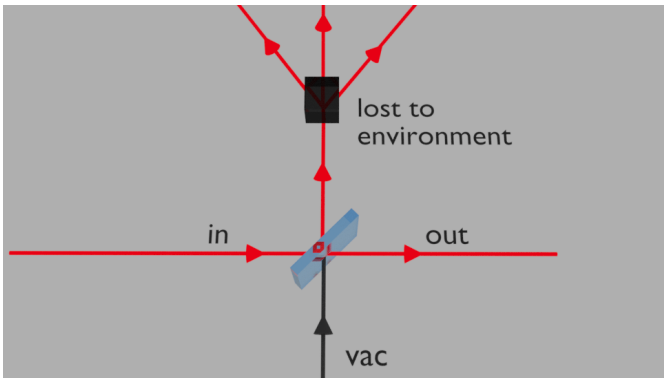

Figure 3.6: Beamsplitter model of attenuation.

The inefficiency of the conversion from light to current is treated as a source of loss, with the attenuation factor called (hamamatsu photonics) the **quantum efficiency** and is given by

$$\eta = \frac{S \times 1240}{\lambda} \times 100[\%]$$

where S $[A/W]$ is the photosensitivity, and λ is the wavelength of the incoming light.

Off-the-shelf photodetectors can usually achieve high quantum efficiencies, but to maximise the measured squeezing it must be near ideal. Therefore most detectors are required to be custom-built.

3.3.3 Dielectric Coating

Laser line highreflective/antireflective optical components can be made by using fused silica substrates coated with multiple layer of dielectrics. The thinkness of each layer then determines whether the reflected fields interfere constructively or destructively, with the former corresponding to highreflective coatings and the latter to antireflective coatings.

These coatings can be done by thin-film deposition, for instance vapour deposition and ion beam sputtering.

None of these techniques can be perfect. There will in general be unwanted scattering and absorption which are treated as loss.

3.3.4 Optical Coherence

When two beams combine at a beamsplitter, the two modes may not interfere properly due to differing polarisations, spatial modes, and wavefront curvatures.

The degree of interference is given by the **mode-matching efficiency**. [17]

3.3.5 Squeezing Purity

Real squeezing employing optical cavities will necessarily suffer from losses in the optics which will affect the squeezing level and its purity. Such an inefficiency is modelled through optical

attenuation, with the amplitude efficiency given by the escape efficiency η_{esc}.

3.3.6 Laser Noise

Lasers suffer from low frequency noise such as relaxation oscillations. Fortunately, it is shot noise limited at higher frequencies. Therefore modulations above that are capable of producing coherent states.

3.3.7 Homodyne Detection

Homodyne with efficiency η is equivalent to having a beam splitter of transmission η directly preceeding perfect detection. The efficiency η is the product of mode-matching efficiency and photodiode quantum efficiency.

3.3.8 Shot Noise and Dark Noise

When the photodetection process converts light into electric current, it will also add classical noise. The noise added is called **dark noise**, which is defined as the noise in the photocurrent in the absence of incident illumination.

We give a brief description of the different sources of noise involved in the photodetection process. Instead of an abstract discussion, it will be much more convenient to explain how each noise can be measured. Consider fig.3.7 illustrating the construction of a homodyne detection system.

In the first part, there is no incident illumination. However, the output photocurrent is non-zero; such a current is termed dark current and the noise it exhibits is called dark noise. This current originates from the thermal fluctuations in the photodiode. The graph displays its spectrum as viewed from a spectrum analyser.

In the middle one, the local oscillator has been injected into the system while the signal port remains blocked. The photodetectors now register electric currents, and the noise level increases on the spectrum analyser. This noise corresponds to the quantum shot noise at the vacuum port, which has been amplified by the local oscillator[9]

Note that the difference between the dark noise level and shot noise level is often called the **dark noise clearance**. This is an experiental inefficiency, and is modelled by an additional noise operator added to the photocurrent.

Alternative terms for dark noise are *electronic noise* and *noise floor*.

[9]For details see the section on homodyning.

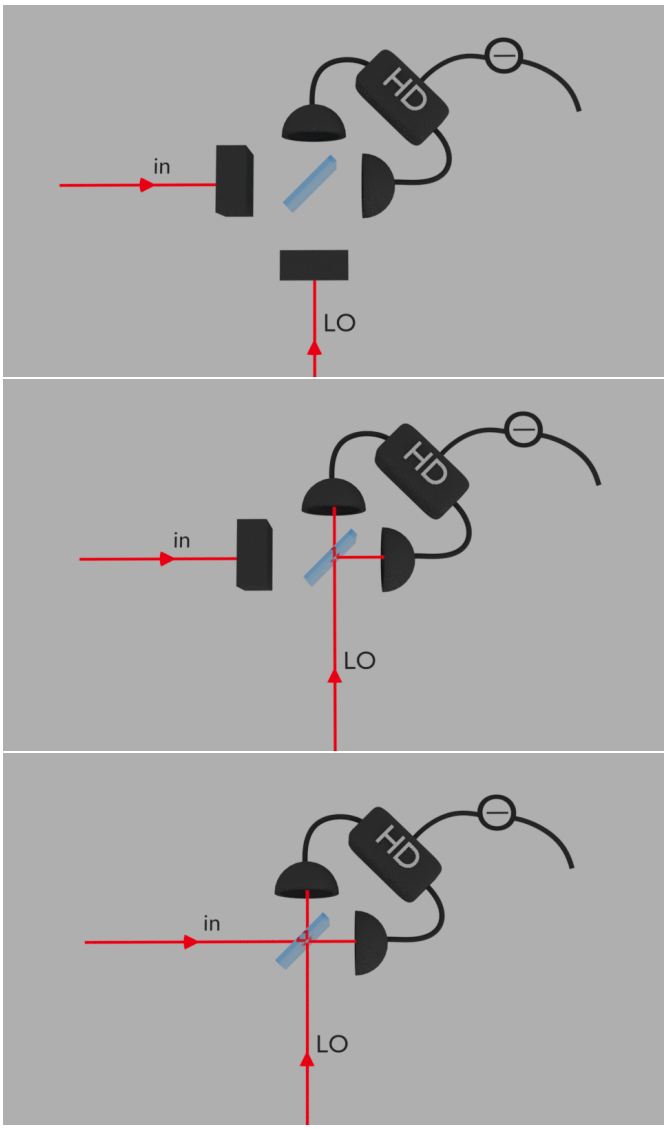

Figure 3.7: Setting up of a homodyne. In terms of measuring the variance: Top- dark noise only. Middle- vacuum shot noise amplified by local oscillator. Bottom- signal measured.

3.4 Electronics and Other Systems

3.4.1 Cavity Locking

Without external control of the mirrors, the cavity will not stay on resonance due to mechanical drift. A brief description of the feedback control loop implemented for locking the cavity length shall be given, based on [4][10].

1. Phase modulation: This effectively varies the frequency of the light. One can determine whether the cavity is blue or red detuned by comparing the sweep and the cavity response.

2. Photodetection: The cavity converts the frequency modulation into amplitude modulation, which can be picked up by a photodetector.

3. Mixer: This facilitates the comparison between the sweep and the cavity response through demodulation using the local oscillator. The result is a DC error signal which can be isolated via a low pass filter.

4. PID control: The proportional-integral-differential controller derives an *error value* from the error signal, which accounts for past accumulations, present, and future predictions of the error.

5. Piezo-amplifier: This actuates the mirror according the the error value delivered.

An experimental generated error signal of the SHG cavity is shown in

3.4.2 Peltier device

The Peltier device is capable of heating or cooling based on a thermoelectric principle called the **Peltier effect**.

The electrons have different energies in each of two semiconductors at an electrical junction. When an electric current is driven through the junction, the electrons either gain or lose energy. This difference in energy results in heat dissipation on one side, and heat absorption on the other. By controlling the direction of the current one can switch between heating and cooling.

The Peltier device was employed in the squeezer cavity to provide temperature actuation of the nonlinear crystal.

4 Generation of Squeezed Light

4.1 Optical χ_2 Non-Linearity

From the Maxwell equations 2.1, one obtains the wave equation of the electric field in dielectric media

$$\boldsymbol{\nabla}^2 E - \frac{1}{c^2}\frac{\partial^2 E}{\partial t^2} = \mu_0 \frac{\partial^2 P}{\partial t^2} \tag{4.1}$$

For linear media, the polarisation is expressed as

$$P = \epsilon_0 \chi E \tag{4.2}$$

and the wave equation is also linear in the electric field. Thus different frequencies of the electric field do not interact.

More generally, most materials behave as **nonlinear media** where the electric polarisation is nonlinear in the electric field[10], viz.

$$P = \epsilon_0(\chi E + \chi_2 E^2 + \cdots) \tag{4.3}$$

This results in a nonlinear wave equation for the electric field, which facilitates mixing between distinct frequencies. A monochromatic electric field would induce multiple frequency components in the polarisation through equation 4.3, which feeds back through the wave equation 4.1 and results in a polychromatic electric field.

Examples of nonlinear optical phenomena which we will encounter includes **second harmonic generation** (SHG) and **squeezing**. The nonlinear optical devices producing these phenomena are the **second harmonic generator** and **optical parametric oscillator** (OPO) shown in fig. 4.1. The second harmonic generator converts a fundamental field of frequency ω into its second harmonic at frequency 2ω. The optical parametric oscillator converts the second harmonic field into lower signal and idler frequencies ω_s and ω_i with $\omega_s + \omega_i = 2\omega$. [20]

One can also **seed** the OPO by injecting the fundamental field into the input. The second harmonic acts like a **pump**, and operation below threshold allows amplification/de-amplification of the fundamental through downconversion/upconversion processes $\omega + \omega \leftrightarrow 2\omega$. We will call such a device the **degenerate optical parametric amplifier** (OPA).

4.2 The Squeezing Mechanism

In section 2.4.2 a quantitative description of squeezing was given in terms of the associated quantum state and transformations. However, it will also be very useful to have a qualitative picture which provides intuition on optical squeezing.

[10] A full spatial description will require tensors. [25]

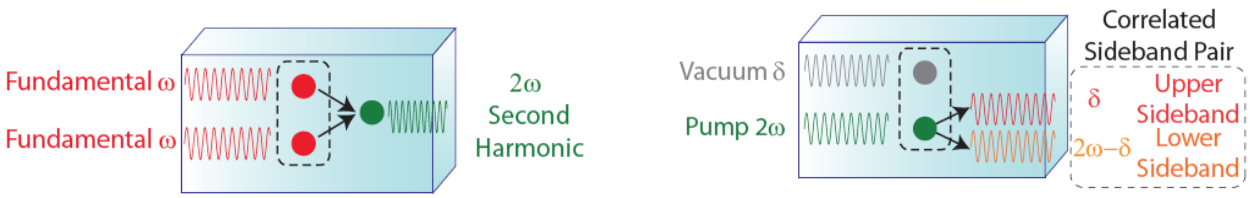

Figure 4.1: Second harmonic generation (left) and optical parametric oscillation (right). Reproduced from [22]

In this section we consider two levels: the macroscopic and microscopic.

It is common to use optical cavities to squeeze light fields. The particular configuration which we shall adopt is the optical parametric amplifier. It turns out that a classical description of the OPA suggests the possibility of squeezing, even without any reference to quantum noise.

The transformation of the OPA can be described in terms of time evolution equations of amplitude and phase operators, and a plot of the phase portrait is given in fig. 4.2 The effect of the OPA is **amplification of a particular field quadrature and de-amplification of the orthogonal quadrature**. It turns out that this behavior is not limited by quantum noise. More precisely, the quantum noise can also be amplified (anti-squeezing) or de-amplified (squeezing), thus transforming coherent states to squeezed states.

While classical arguments can motivate squeezing, it cannot provide a complete description. Squeezing at the microscopic level can be described as **entanglement between sidebands**. For a *coherent state*, the sidebands are phasors which fluctuate *independently*. These vacuum fluctuations is what gave rise to quantum shot noise. For a *squeezed state*, the upper and lower side bands are *correlated*.

Concretely, the variance of the RF signal quadrature translates through equation 2.30 directly into the entanglement criterion [11][6] involving the upper and lower sideband quadratures. The entanglement is EPR-like.

The first type of correlation given by

$$\hat{x}(\Omega) + \hat{x}(-\Omega) \to 0 \tag{4.4}$$

$$\hat{p}(\Omega) - \hat{p}(-\Omega) \to 0 \tag{4.5}$$

give rise to amplitude squeezing

$$\langle \Delta \hat{x}^2_{sig} \rangle \to 0 \tag{4.6}$$

In terms of the sideband diagram the correlations resemble that of classical phase modulation. Thus interference between the side bands results in noise reduced from the amplitude quadrature and added to the phase quadrature.

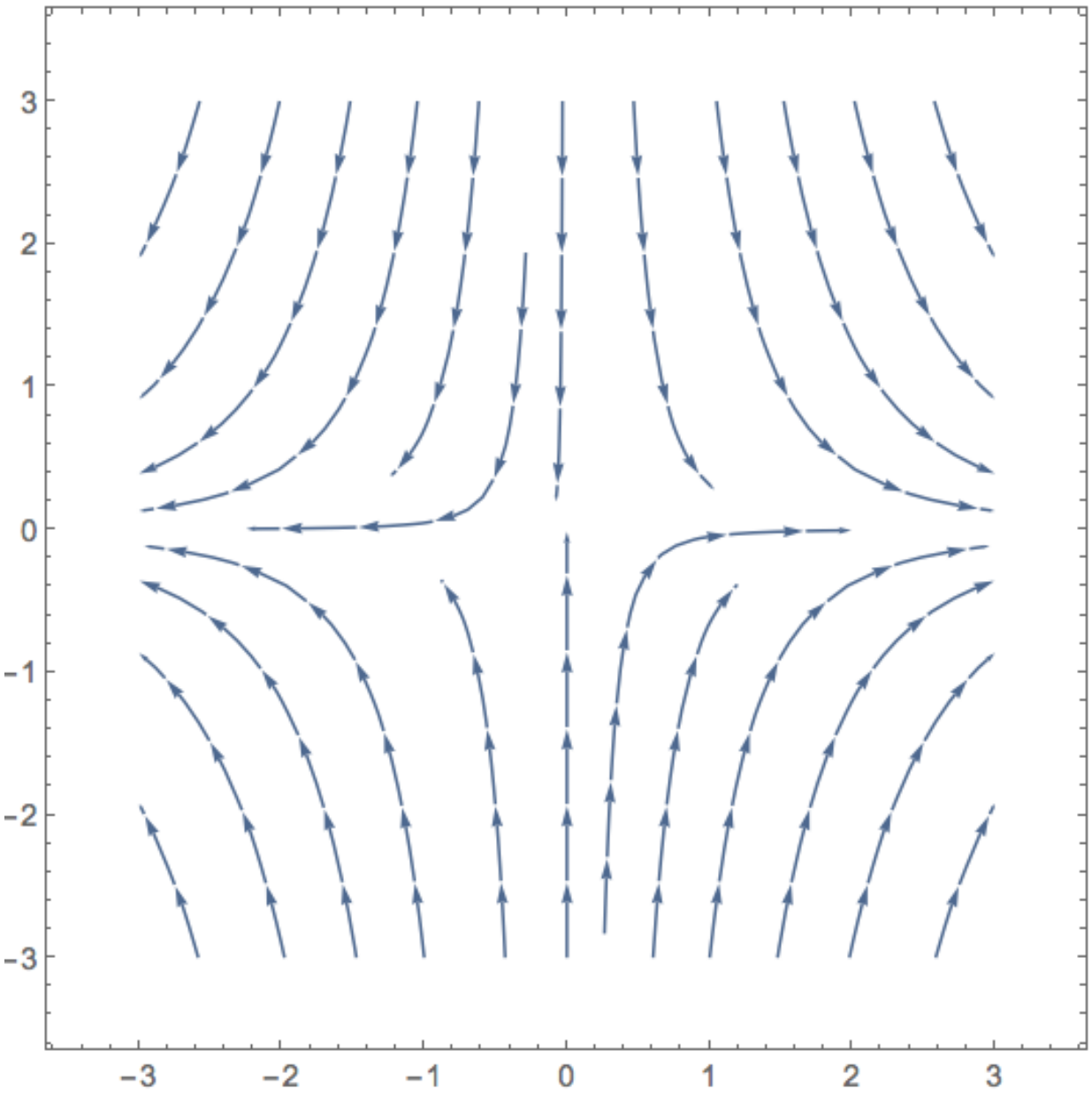

Figure 4.2: Classical phase portrait of the OPO. Indicates amplification and deamplification.

Similarly, we have a second type of correlation given by

$$\hat{x}(\Omega) - \hat{x}(-\Omega) \to 0 \tag{4.7}$$

$$\hat{p}(\Omega) + \hat{p}(-\Omega) \to 0 \tag{4.8}$$

This corresponds to phase squeezing

$$\langle \Delta \hat{p}^2_{sig} \rangle \to 0 \tag{4.9}$$

with a sideband diagram similar to that of classical amplitude modulation.

Specifically, we will be using the vacuum seeded OPA for generating vacuum squeezing. The entanglement thus originates from the vacuum seeded downconversion process which generates entangled sidebands (fig. 4.1)

4.3 Cavity Equations

We shall review the quantitative model of the squeezer cavity, and the SHG cavity required for pumping the squeezer. It will be based on [8] and [22] and the beginning point will be the quantum Langevin equations for a general ring cavity given in Eq. 3.8

4.3.1 Second Harmonic Generator

The second harmonic generator converts the input fundamental field at 1550nm into its second harmonic at 775nm. This process can be described in classical optics, which simplifies the quantum Langevin equations to include only classical terms

$$\dot{\alpha} = -\kappa_a \alpha + \epsilon \alpha \beta + \sqrt{2\kappa^a_{in}} A_{in} \tag{4.10}$$

$$\dot{\beta} = -\kappa_b \beta - \frac{\epsilon}{2} \alpha^2 \tag{4.11}$$

Under a steady state assumption, one may solve for the intra-cavity second harmonic field amplitude and infer the output field amplitude through boundary conditions to obtain

$$\beta_{out} = \frac{\sqrt{2\kappa^b_{out}} \epsilon \alpha^2}{2\kappa_b} \tag{4.12}$$

Roughly speaking, the second harmonic field increases with increasing output coupling and decreasing circulation losses.

4.3.2 Classical Optical Parametric Amplifer

Although a quantum theory of the OPA is required to describe squeezing, classical formulations can help to elucidate properties of the OPA.

To begin with, we shall **neglect pump depletion** and ignore the $\epsilon\hat{a}^2/2$ term. Furthermore, we shall also approximate the pump field by a classical complex amplitude. The equation of motion of the fundamental field under such assumptions becomes

$$\dot{\hat{a}} = -\kappa_a \hat{a} + g\hat{a}^\dagger + \sqrt{2\kappa_{in}^a}\hat{A}_{in} + \sqrt{2\kappa_{out}^a}\hat{A}_{out} + \sqrt{2\kappa_l^a}\hat{A}_l \tag{4.13}$$

with $g = \epsilon b$.

The classical OPA should correspond to the case when one ignores the quantum noise:

$$\dot{\alpha} = \kappa_a \alpha + g\overline{\alpha} + \sqrt{2\kappa_{in}^a}A_{in} \tag{4.14}$$

To solve this equation, we could mimick the treatment of the SHG by assuming a steady state. Decomposing the amplitude into quadratures $\alpha = x + ip$ results in

$$x = \frac{\sqrt{2\kappa_{in}^a}x_{in}}{\kappa_a - g} \tag{4.15}$$

$$p = \frac{\sqrt{2\kappa_{in}^a}p_{in}}{\kappa_a + g} \tag{4.16}$$

$$\tag{4.17}$$

where we have assumed that g is real. The OPA therefore amplifies the amplitude quadrature while de-amplifying the phase quadrature. More generally, changing the pump phase and therefore the phase of g will change the bases where amplification and de-amplification occurs.

One can also find a singularity at $g = \kappa_a$, which is to say

$$b = \frac{\kappa_a}{g} \tag{4.18}$$

The pump power corresponding to this singularity is known as the **threshold power**. The assumption of pump non-depletion breaks down near this point and beyond.

4.3.3 Squeezer

The **vacuum squeezer** is simply a **vacuum seeded OPA**. In this case, one may assume a non-depleting classical pump but is forbidden to ignore the quantum noise. Equation 4.13 therefore directly describes the squeezer cavity.

Similar to the classical OPA, this decomposes into equations for the amplitude and phase quadratures

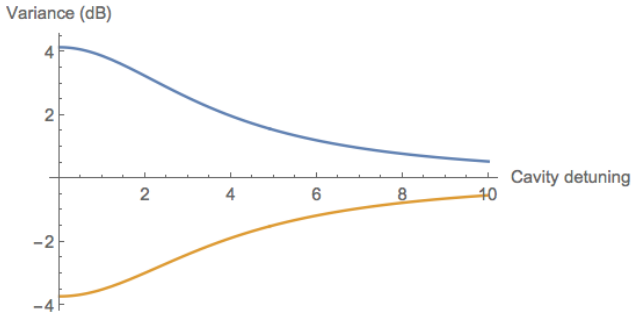

Figure 4.3: Dependence of squeezing on cavity detuning. Noise normalised to SNL. Squeezing bandwidth is finite due to cavity filtering properties.

$$\dot{\hat{x}} = (-\kappa_a + g)\hat{x} + \sqrt{2\kappa^a_{in}}\hat{x}_{in} + \sqrt{2\kappa^a_{out}}\hat{x}_{out} + \sqrt{2\kappa^a_l}\hat{x}_l \tag{4.19}$$

$$\dot{\hat{p}} = (-\kappa_a - g)\hat{p} + \sqrt{2\kappa^a_{in}}\hat{p}_{in} + \sqrt{2\kappa^a_{out}}\hat{p}_{out} + \sqrt{2\kappa^a_l}\hat{p}_l \tag{4.20}$$

Upon Fourier transformation and application of boundary conditions, one arrives at the expressions for the output quadratures

$$\hat{x}_{out} = \frac{(2\kappa^a_{out} - i\omega - \kappa_a + g)\hat{x}_\nu + \sqrt{4\kappa^a_{in}\kappa^a_{out}}\hat{x}_{in} + \sqrt{4\kappa^a_l\kappa^a_{out}}\hat{x}_l}{i\omega + \kappa_a - g} \tag{4.21}$$

$$\hat{p}_{out} = \frac{(2\kappa^a_{out} - i\omega - \kappa_a - g)\hat{p}_\nu + \sqrt{4\kappa^a_{in}\kappa^a_{out}}\hat{p}_{in} + \sqrt{4\kappa^a_l\kappa^a_{out}}\hat{p}_l}{i\omega + \kappa_a + g} \tag{4.22}$$

The variance is therefore given by

$$\langle \Delta\hat{x}^2_{out} \rangle = 1 + \frac{\kappa^a_{out}}{\kappa_a} \frac{4g/\kappa_a}{(\omega/\kappa_a)^2 + (1 - g/\kappa_a)^2} \tag{4.23}$$

$$\langle \Delta\hat{p}^2_{out} \rangle = 1 - \frac{\kappa^a_{out}}{\kappa_a} \frac{4g/\kappa_a}{(\omega/\kappa_a)^2 + (1 + g/\kappa_a)^2} \tag{4.24}$$

and the dependence on cavity detuning is illustrated in fig. 4.3.3. Amplification and deamplification now corresponds to antisqueezing and squeezing respectively. The **squeezing bandwidth** is finite due to the finite cavity bandwidth.

It is important to note that the squeezing is always impure. The **escape efficiency** defined through

$$\eta_{esc} = \frac{\kappa^a_{out}}{\kappa_a} \tag{4.25}$$

approximately describes the loss of the squeezed field before exiting the cavity.

4.4 Cavity Design

4.4.1 Geometry

The most general division of optical cavities corresponds to whether they support travelling waves or standing waves.

In a **travelling wave** design, the field does not interfere with itself until after one round trip; such cavities are **ring** cavities with the back-reflection exiting the cavity at the different angle to the forward propagating beam.

On the other hand, the intra-cavity field will overlap itself within each round trip in a **standing wave** design; these cavities are usually **linear**, with the optical path of the back-reflection coincident with the forward propagating field.

The advantages of a standing wave design is threefold:

1. Reduced intra cavity loss due to less contact surfaces over each round trip. Minimising intra-cavity losses is crucial in squeezing experiments, since the escape efficiency is inversely proportional to the total intra-cavity loss (eq.4.25)

2. Mechanical stability due to compact geometry.

3. Minimal astigmatism and ellipticity since all angles of incidence are normal.

On the other hand, the **bowtie cavity** which supports travelling waves would allow for

1. Flexibility through optimisation of the many degrees of freedom (mirror separations, angles, etc.)

2. Accessibility due to increased number of ports for locking/pumping.

3. Backscatter isolation since optics are not at normal incidence.

Back-reflected light can also be reflected again from other upstream optics towards the squeezer cavity, which could act as a seed and thereby degrading the squeezing.

It is worth noting that mirror reflectivities could be near ideal, therefore one does not need to worry about adding the extra mirror or two. The intra-cavity loss is dominated by the AR coatings and absorption of the crystal.

4.4.2 Mirror Specifications

Bowtie cavities branch further into two types: singly or doubly resonant.

Doubly resonant cavities support simultaneous resonance of the fundamental and second harmonic, which allows for three advantages:

- Reduced threshold due to resonant pump.

- Additional control field from the resonant second harmonic.
- Ease of mode-matching between the interacting fundamental and second harmonic through mode-matching to the cavity.
- Spatial filtering of the second harmonic by the cavity, which reduces photothermal effects.

While double resonance possess many theoretical advantages, it is also very difficult to implement experimentally. Examples of disadvantages include:

- Photothermal effects due to resonantly-enhanced second harmonic.
- Reduced phase-matching bandwidth constrained by the temperature bandwidth of the nonlinear interaction, and also due to intra-cavity dispersion from temperature changes.
- Sensitive to intra-cavity dispersion.

On the other hand, **singly resonant** cavities which allow resonant fundamental and single pass second harmonic is simple to implement. It therefore solves many of the problems introduced through the complexities of double resonance. We have adopted the singly resonant cavities for this reason. Experimentally, this means that the cavity mirrors are generally high reflective for the fundamental but high transmittive for the second harmonic.

The OPA escape efficiency η_{esc} and threshold power β_{th} were given in eq.4.18 and 4.25 by

$$\eta_{esc} = \frac{\kappa_{out}}{\kappa} \tag{4.26}$$

$$\beta_{th} = \frac{\kappa}{g} \tag{4.27}$$

This results in a dilemma regarding the intra-cavity loss:

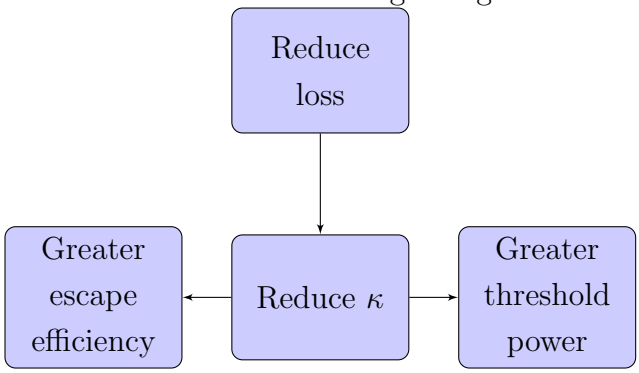

Increasing loss leads to the opposite problem of having reduced threshold but reduced escape efficiency as well. The loss of our cavity was such that κ is sufficiently small to be accessible by our powerful laser, but κ_{out} sufficiently large ($R_{out} = 90\%$) to achieve high escape efficiency.

The curvatures of and separations between the mirrors were designed in order to optimise the beam waist. An optimal waist for maximising the nonlinear interaction has been described in ref

Finally, all mirrors have been superpolished to minimise scattering.

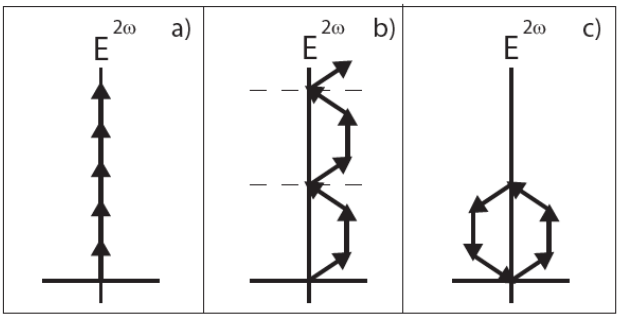

Figure 4.4: a)Phase matched. b)Quasi-phase matching c) Phase mismatched. Figure reproduced from [22]

4.4.3 Crystal Design

In order to access the second order interaction, it is important that the fundamental and second harmonic are **phase-matched**. More generally, ideal interaction requires the conservation of 4-momentum

$$\begin{bmatrix} \hbar\omega \\ \hbar\mathbf{k} \end{bmatrix} = \begin{bmatrix} \hbar\omega_1 \\ \hbar\mathbf{k}_1 \end{bmatrix} + \begin{bmatrix} \hbar\omega_2 \\ \hbar\mathbf{k}_2 \end{bmatrix} \tag{4.28}$$

The first condition corresponds to conservation of energy. The second condition corresponds to momentum conservation when viewed in terms of photons, and corresponds to phase matching when viewed in terms of waves.

Energy conservation is a physical law which restricts the possible interaction processes. Phase matching is more of an experimental requirement; phase mismatch does not forbid the occurrence of a given process but will reduce the efficiency. A detailed discussion of phase matching is given later in this section using the example of second harmonic generation.

Phase mismatch occurs due to material dispersion, with a condition on the refractive indices corresponding to two interacting wavelengths

$$n_{pump} = n_{seed} \tag{4.29}$$

As an example, consider the case of second harmonic generation. In terms of phasors, ideal phase matching allows the second harmonic field generated at different points along the optical axis to interfere constructively 4.4. When phase mismatched, the second harmonic fields can interfere destructively as the phase difference accumulates.

Two common techniques for improving phase matching are **quasi-phase matching** and **birefringent phase matching**.

Birefringent phase matching involves a crystal demonstrating *birefringence*, which allow for variation in the refractive indices through changing the angle of incidence and temperature. The

disadvantage of this method is the stringent conditions imposed on the experimental setup. ref

On the other hand, quasi-phase matching preserves these experimental degrees of freedom at the expense of the phase matching efficiency. Concretely, **periodic poling** flips the sign of χ_2 at given intervals. This is equivalent to a π phase shift on the second harmonic generated through the χ_2 interaction, and hence improves the constructive interference as seen in the phasor diagram.

Without phase matching, optimal constructive interference occurs at intervals of length

$$L_c = \frac{\pi}{|\Delta k|} \tag{4.30}$$

called the **coherence length**, inversely proportional to $\Delta k = \mathbf{k}_3 - \mathbf{k}_2 - \mathbf{k}_1$ which measures phase mismatch. At this point destructive interference begins to occur; perfect destructive interference occurs at the next integer multiple of the coherence length. Optimal quasi-phase matching is therefore limited to the size of the coherent length; poor phase matching leads to short coherent lengths for which periodic poling may be difficult to do.

The primary factor for the choice of material is loss due to scattering and absorption. Periodically poled potasisum titanyl phosphate (PPKTP) is thus particularly suitable, with an even less absorption coefficient at 1550nm. [23]

Finally, it is worth noting that the **damage threshold** of PPKTP is sufficiently higher than the operating regimes of the OPA cavity. At lower powers, one may already run into trouble with photothermal effects due to the heating from the pump.

4.4.4 Pump Field

The pump was generated from the SHG cavity, which is also a bowtie with exactly the same specifications as the squeezer cavity. This is because the squeezer cavity was designed for efficient and convenient nonlinear interaction, therefore the same principle applies to SHG. Instead of vacuum seeded frequency downconversion (squeezing), the SHG runs on frequency doubling seeded by the fundamental field.

4.5 Experiments and Results

The experimental component of this honours project comprised of a single month of labwork in the newly established 1550nm lab. This involved setting everything up from scratch.

Although the final goal is the construction of a squeezer, this has not been achieved due to the time constraint. We will therefore present some of the important steps leading up to the squeezer.

To begin with, the SHG cavity is shown in fig.4.5. To characterise the cavity, we measured the second harmonic conversion efficiency as shown in fig. The alignment is near optimal.

Fig.4.6 corresponds to the temperature bandwidth of the nonlinear crystal, showing clearly the square of the sinc function [8]. The bandwidth is quite broad, at a few degrees Celcius;

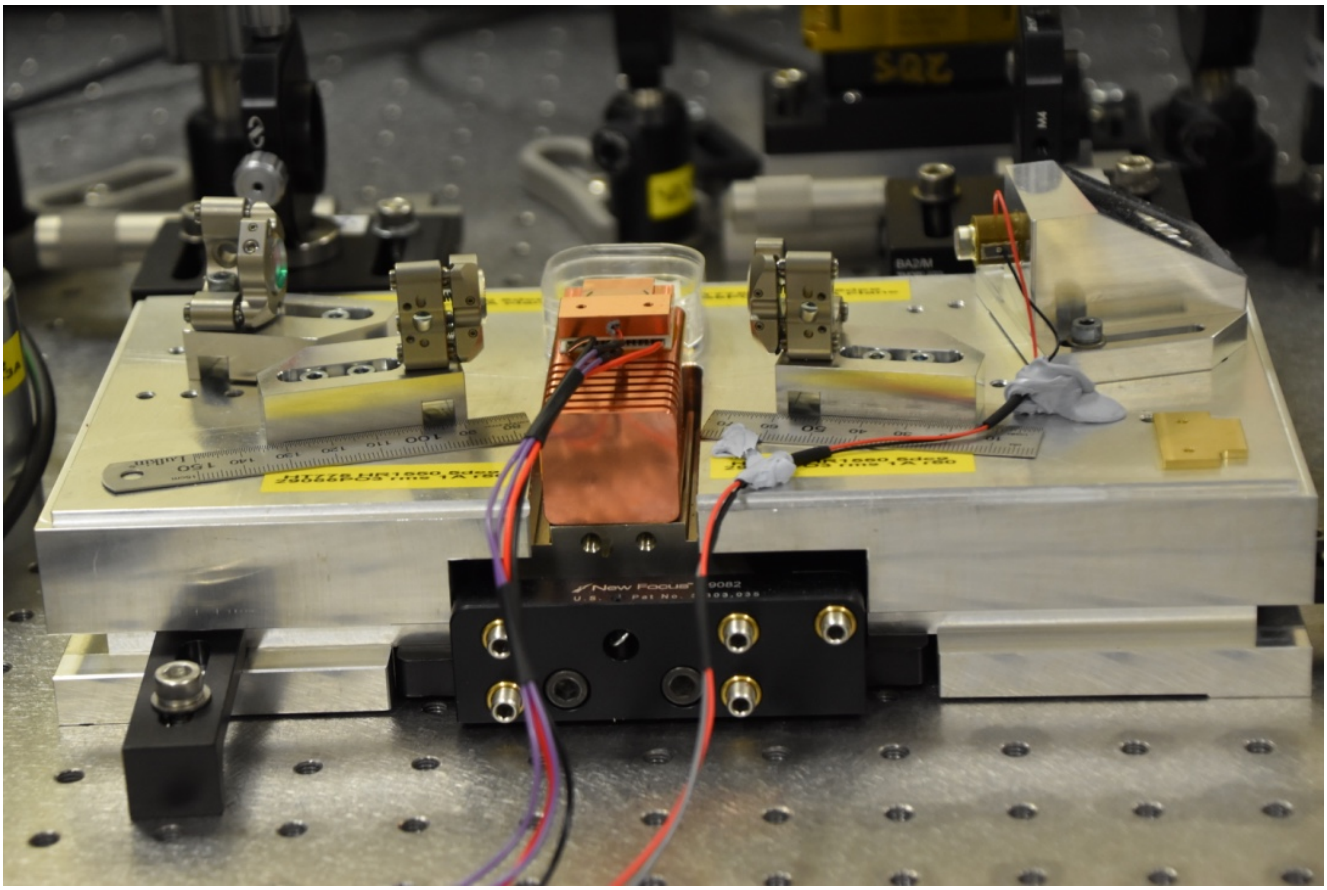

Figure 4.5: Setup of the second harmonic generator.

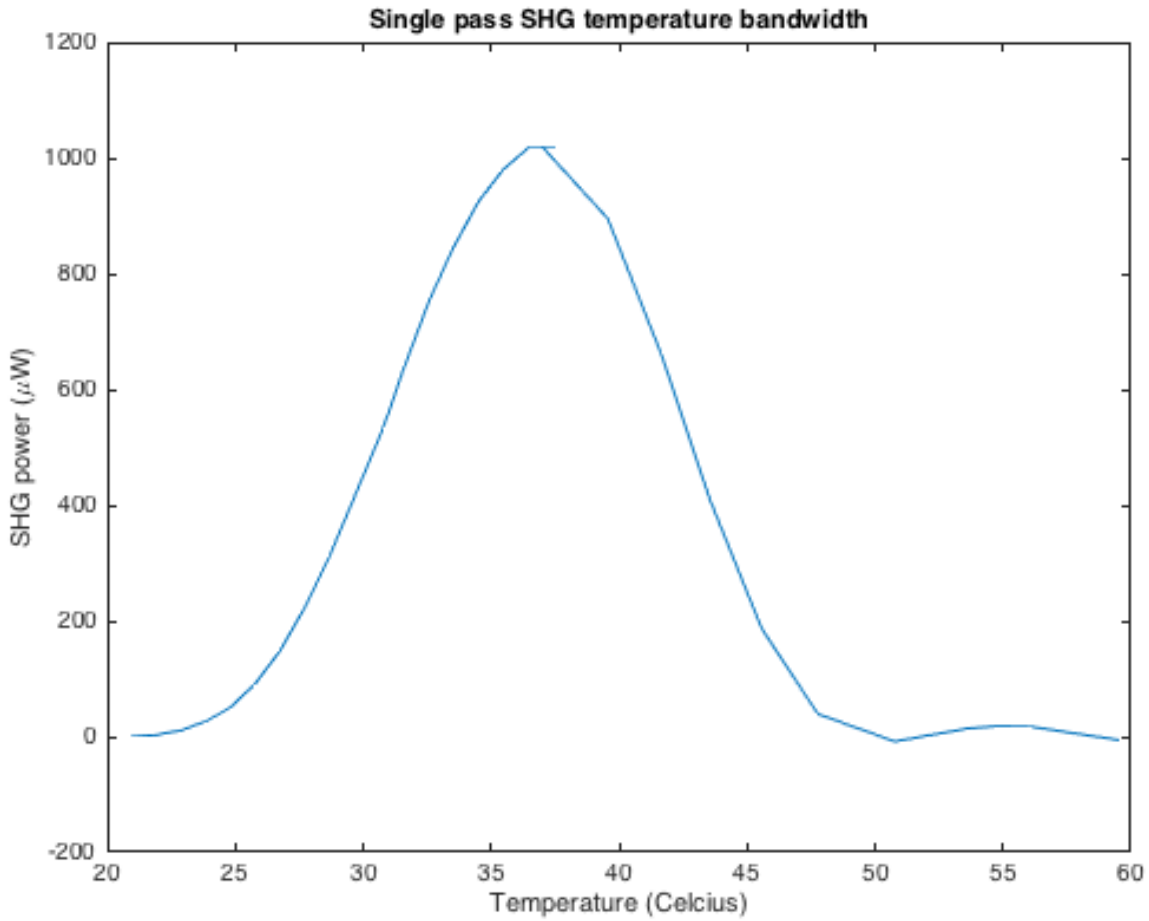

Figure 4.6: Temperature bandwidth of nonlinear interaction.

temperature controllers in the laboratory are capable of accuracies up to micro-Kelvins, allowing stable phase-matching for the nonlinear interaction.

The squeezer cavity is shown in fig.4.7. As discussed in section 4.4.4, both the squeezer and the SHG share the same cavity designs.

Due to time constraints, no squeezing had been observed. However the squeezer cavity has been aligned to the OPA seed, and it remains to couple the pump into the OPA and setup a homodyne detector at the squeezed field output. A trace acquired from the oscilloscope showing the alignment of the squeezer cavity has been given in fig.4.8

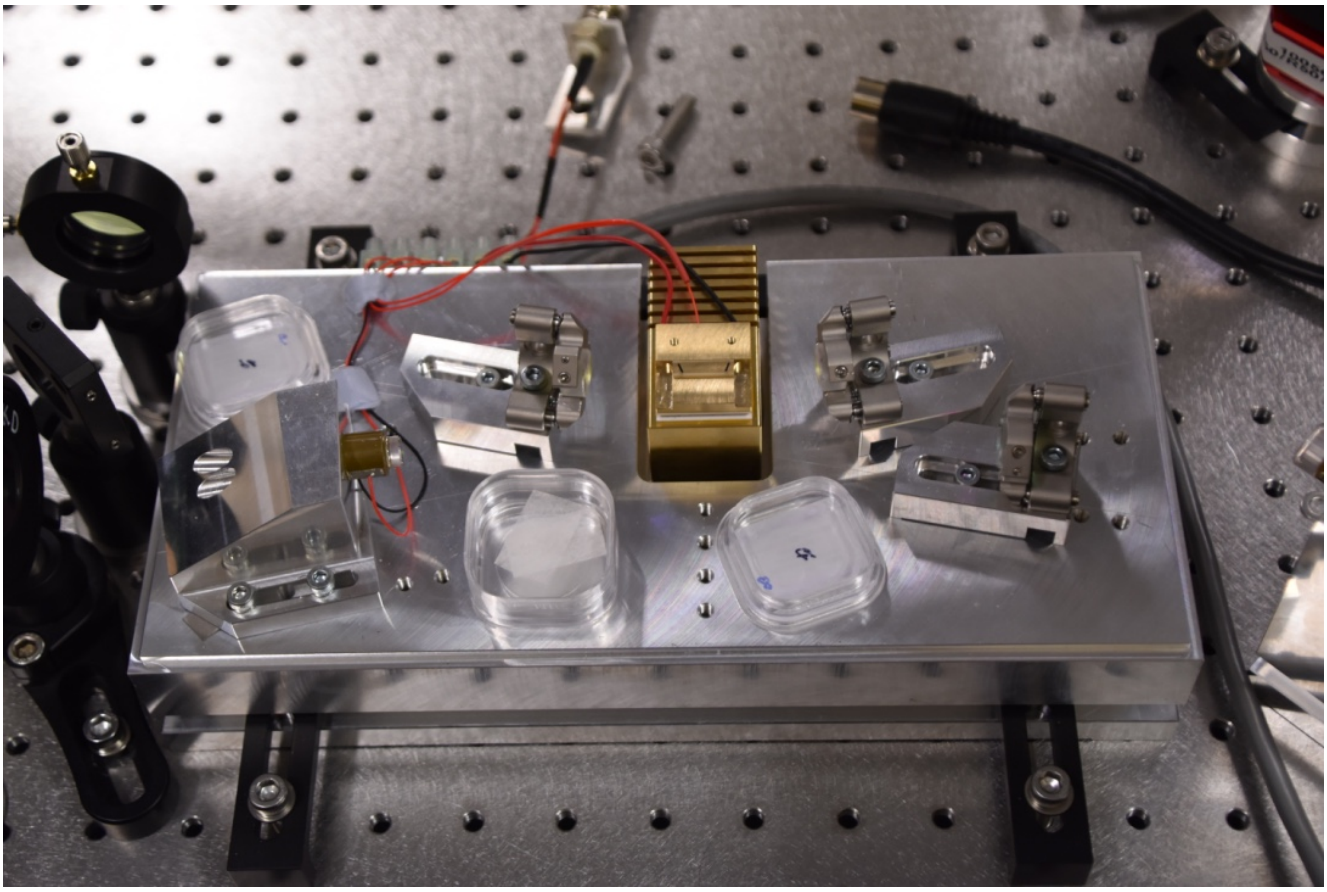

Figure 4.7: Setup of squeezer OPA cavity.

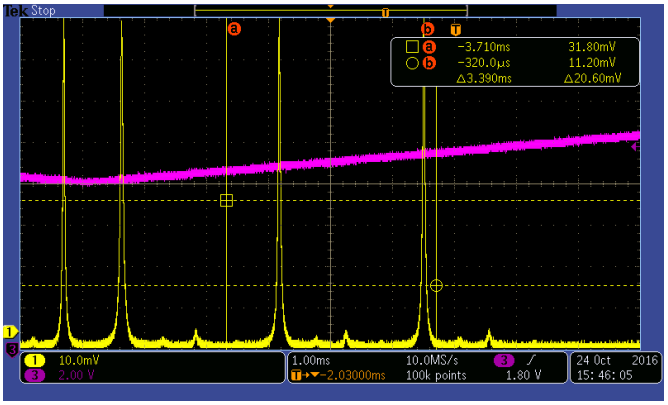

Figure 4.8: A scan of the peaks of the squeezer OPA cavity.

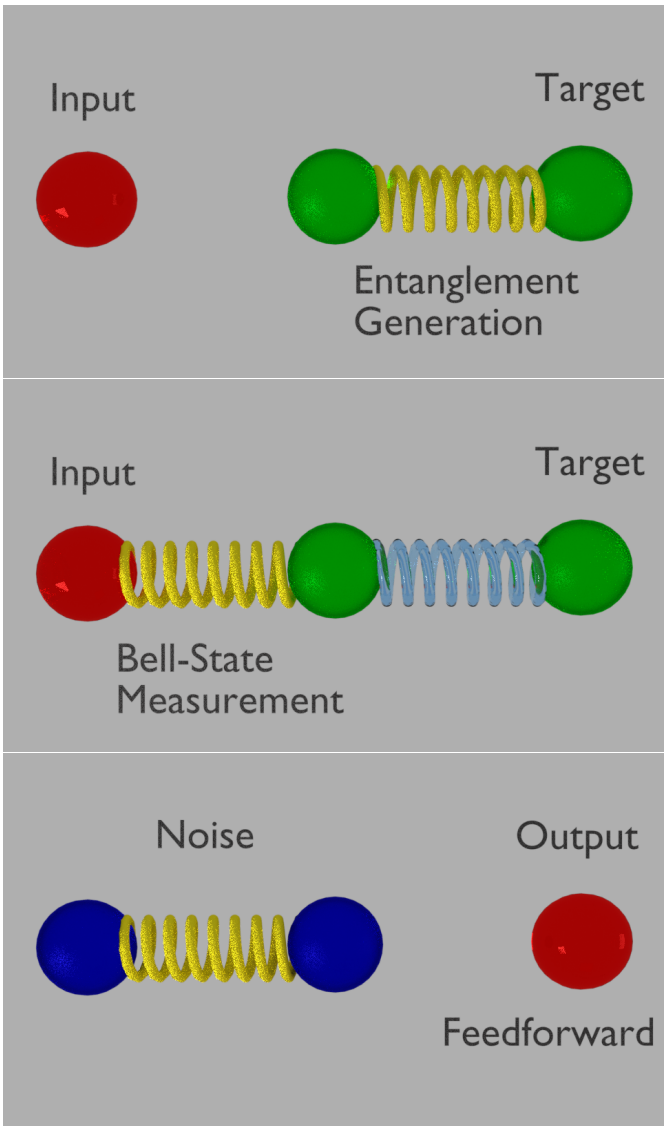

Figure 5.1: Teleportation

5 Quantum State Teleportation

Quantum teleportation is basically a cup-and-string phone with secure cups and without the string.

The fundamental protocol of quantum teleportation (also referred to as state teleportation) is very simple. An illustration is given in

and we shall explain the rough idea with details left for the next section. State teleportation consists of three steps. The first step is **entanglement generation**, which provides the required quantum channel for communication. The second step is coupling of the input state into the channel, done via **Bell-state measurements** which entangle the input state with one side of the pre-entangled resource at the sender station. The correlations established between the input

and target state allow information of the input state to flow to the target state. At this stage, the target state is not identical to the input state. Specifically, it is the input state up to *random displacements* due to the noise in the entanglement, and which depend on the outcome of the Bell-state measurement. Thus the final step required is **feedforward correction**, whence the outcome of the measurement is communicated to the receiver to decrypt the noisy signal and obtain the correct output state.

5.1 Ideal Protocol

5.1.1 Discrete Variable

We shall begin by considering the more intuitive case of qubits. Generalisation to higher finite-dimensional and infinite-dimensional systems will proceed along similar lines.

Suppose the input is an unknown state $|\psi\rangle = \alpha|0\rangle + \beta|1\rangle$, and the entangled resource is $|\Phi\rangle = (|00\rangle + |11\rangle)/\sqrt{2}$. Then the system would be given by the tensor product

$$|\psi\rangle_{\text{input}} \otimes |\Phi\rangle_{\text{entangled resource}} \tag{5.1}$$

which could be decomposed into

$$\begin{aligned}(&\frac{1}{\sqrt{2}}(|00\rangle + |11\rangle)_{\text{Bell-state}} \otimes (\alpha|0\rangle + \beta|1\rangle)_{\text{target}} + \frac{1}{\sqrt{2}}(|00\rangle - |11\rangle)_{\text{Bell-state}} \otimes (\alpha|0\rangle - \beta|1\rangle)_{\text{target}} \\ &+ \frac{1}{\sqrt{2}}(|01\rangle + |10\rangle)_{\text{Bell-state}} \otimes (\alpha|1\rangle + \beta|0\rangle)_{\text{target}} + \frac{1}{\sqrt{2}}(|01\rangle - |10\rangle)_{\text{Bell-state}} \otimes (\alpha|1\rangle - \beta|0\rangle)_{\text{target}})/2\end{aligned} \tag{5.2}$$

Note that the *target state* refers to the output state before the feedforward. It is the object which we wish to teleport the input quantum state onto.

In the formation above, each of the four summands corresponds to a particular outcome of the Bell state measurement. After the measurement, applying the required unitary transformation to the target state reproduces the input state at the receiver station. For example, if the measurement outcome corresponds to the third summand, then:

$$\alpha|1\rangle + \beta|0\rangle \xrightarrow{|0\rangle\langle 1| + |1\rangle\langle 0|} \alpha|0\rangle + \beta|1\rangle = \text{desired output state} \tag{5.3}$$

5.1.2 Continuous Variable

The case for continuous variables is completely analogous to the discrete variable case. If the input is an unknown wavefunction ψ

$$|\psi\rangle = \int dz\ \psi(z)|z\rangle \tag{5.4}$$

and the entangled resource is

$$|\Phi\rangle = \frac{1}{\sqrt{\pi}} \int dx \, |x\rangle \, |x\rangle \tag{5.5}$$

then the system is given by the tensor product of the two, and could be decomposed as

$$|\psi\rangle \otimes |\Phi\rangle = \iint dudv \left(\frac{1}{\sqrt{\pi}} \int dx \; e^{2ixv} \, |x\rangle \, |x+u\rangle \otimes \int dz \; \psi(z) e^{-2izv} \, |z+u\rangle \right) \tag{5.6}$$

The double integral over u and v sums over the continuous variable Bell-state basis. The integrand consists of each Bell-state basis (the first term) in a tensor product with the target state (the second term), which is identical to the input state up to a translation and phase change.

From this decomposition, it is clear that the DV teleportation protocol consisting of entanglement generation, measurement, and feedforward can be adapted easily for the CV case at least in principle.

5.2 Optical Implementation

The ideal teleportation protocols are simple and elegant. Unfortunately they also turn out to be pipe dreams. Discrete variable teleportation (e.g. photon polarisation states) suffers from imperfect Bell-state measurements with non-unit success rates. Continuous variable teleportation (e.g. amplitude and phase quadratures of light) suffers from imperfect entanglement resource, which means that the quantum channel can never be perfect. We will analyse the continuous variable case in depth.

The setup of teleporting optical quadratures is shown in

The entangled resource required is the two-mode-squeezed-state, with the Bell-state measurement performed by dual-homodyning. The measurement results are fed-forward to amplitude and phase modulators which performs the required unitary corrections on the optical quadratures.

5.3 Representations

In this part, we will summarise different formalisms of teleporting optical quadratures. They are of course equivalent, but will be useful in different cases. For example, describing the action of an embedded noiseless linear amplifier in the teleporter will be much simpler in the Schrödinger picture, while performing post-selection on the Bell-state measurement results would be easier to do in the Heisenberg picture.

5.3.1 Heisenberg Picture

This method was used in [14], and turns out to be the most suitable for a conceptual description of the standard teleportation protocol. We shall denote the EPR beams by A and B as in the

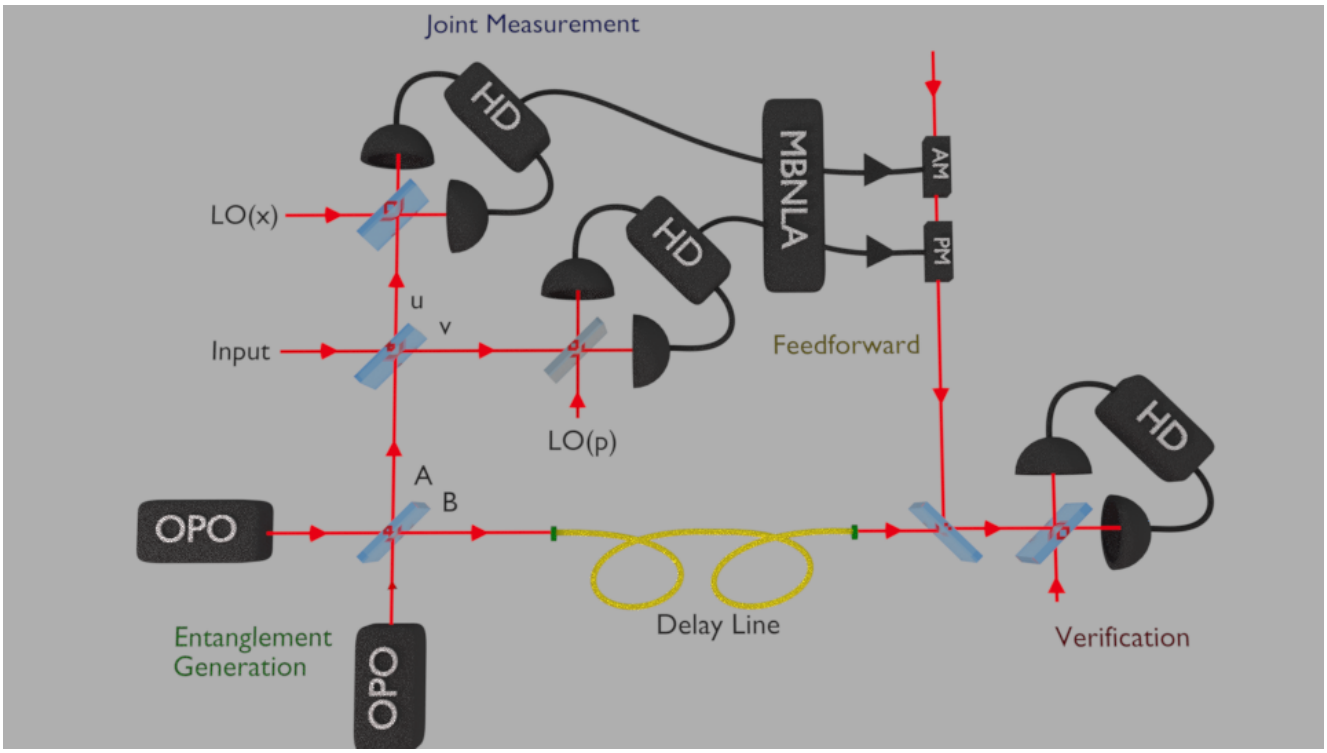

Figure 5.2: Optical teleportation

figure. Then we may write the target state (i.e. before the feedforward) as

$$\hat{x}_B = \hat{x}_A - \sqrt{2}e^{-r}\hat{x}_B^{(0)}$$
$$\hat{p}_B = \hat{p}_A + \sqrt{2}e^{-r}\hat{p}_A^{(0)}$$

Denoting the measured beams by u and v as shown in the figure, then the quadratures will be given by

$$\hat{x}_u = (\hat{x}_{in} - \hat{x}_A)/\sqrt{2} \qquad \hat{p}_u = (\hat{p}_{in} - \hat{p}_A)/\sqrt{2}$$
$$\hat{x}_v = (\hat{x}_{in} + \hat{x}_A)/\sqrt{2} \qquad \hat{p}_v = (\hat{p}_{in} + \hat{p}_A)/\sqrt{2}$$

and the dual-homodyne performs the Bell-state measurement by measuring $\hat{x}_u$ and $\hat{p}_v$. With this in mind, we may rewrite the target state as

$$\hat{x}_B = \hat{x}_{in} - \sqrt{2}e^{-r}\hat{x}_B^{(0)} - \sqrt{2}\hat{x}_u$$
$$\hat{p}_B = \hat{p}_{in} + \sqrt{2}e^{-r}\hat{p}_A^{(0)} - \sqrt{2}\hat{p}_v$$

After the measurement, the operators $\hat{x}_u$ and $\hat{p}_v$ collapse to single numbers, and therefore we may feedforward the result to the modulators to perform the displacements $+\sqrt{2}x_u$ on $\hat{x}_B$ and $+\sqrt{2}p_v$ on $\hat{p}_B$ to obtain the final teleporter output:

$$\hat{x}_{tel} = \hat{x}_{in} - \sqrt{2}e^{-r}\hat{x}_B^{(0)}$$
$$\hat{p}_{tel} = \hat{p}_{in} + \sqrt{2}e^{-r}\hat{p}_A^{(0)}$$

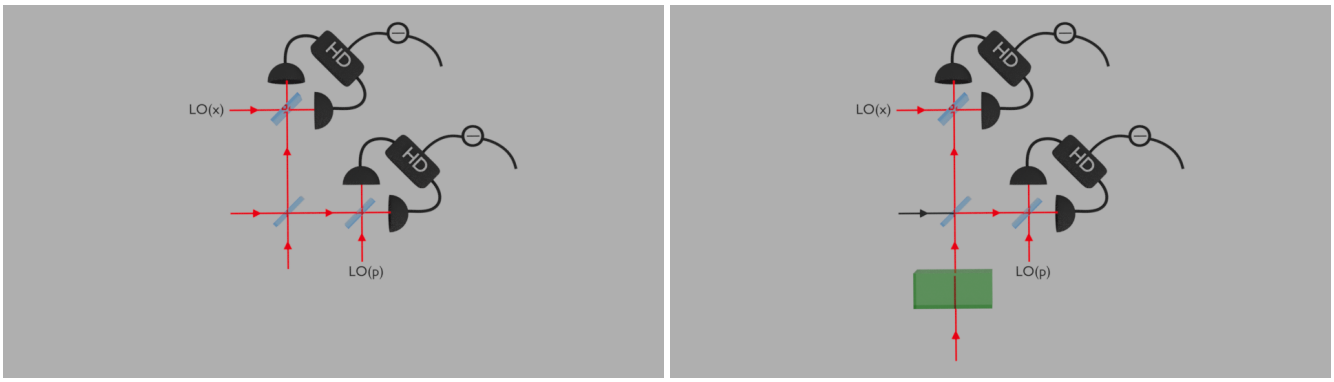

Figure 5.3: Displacement shifting

The output state then has the same complex amplitude as the input coherent state but with additional noise, which depends only on the amount of squeezing available for producing the entangled resource. In the limit of perfect squeezibg ($r \to \infty$), the teleported state approaches the input state.

5.3.2 Schrödinger Picture

This has the advantage of tracking quantum states explicitly (coherent states, thermal states, etc.) This picture is useful for the NLA, but not so much for modelling inefficiencies.

Consider once again the same teleporter setup, with the same notations. To simplify the Bell-state measurement, we can mathematically shift the input coherent state from one port of the beam-splitter to the other input port. The equivalence between the two picture is depicted in fig. 5.3 and is much more convenient because the dual-homodyne is now equivalent to heterodyne on the single (non-vacuum) input port, which is simply a coherent projection.

A straightforward calculation with the input displacement and conditioning on a Bell-state measurement result of $|\gamma\rangle$ results in the output state described by the density operator (unnormalised)

$$\hat{\rho}(\gamma) = \langle\gamma|_A \hat{D}_A(-\overline{\alpha}) |TMSS\rangle \langle TMSS| \hat{D}_A^\dagger(-\overline{\alpha}) |\gamma\rangle_A \tag{5.7}$$

$$= (1-\lambda^2) e^{(-(1-\lambda^2)|\gamma+\overline{\alpha}|^2)} |\lambda(\overline{\gamma}+\alpha)\rangle \langle\lambda(\overline{\gamma}+\alpha)| \tag{5.8}$$

The measurement result is fed-forward with an electronic gain of g to the modulators, and a displacement of $\hat{D}_B(-g\overline{\gamma})$ applied to the EPR mode B. The ensemble statistics of the teleporter output would then be given by

$$\hat{\rho}_{tel} = \int d\gamma \; \hat{D}_B(g\gamma) \langle\gamma|_A \hat{D}_A(-\overline{\alpha}) |TMSS\rangle \langle TMSS| \hat{D}_A^\dagger(-\overline{\alpha}) |\gamma\rangle_A \hat{D}_B^\dagger(g\gamma) \tag{5.9}$$

$$= \frac{1-\lambda^2}{(g-\lambda)^2} \int d\xi \; \exp\left(-\frac{1-\lambda^2}{(g-\lambda)^2}|\xi - g\alpha|^2\right) |\xi\rangle \langle\xi| \tag{5.10}$$

where the change of variable is given by $\xi = \lambda(\overline{\gamma} + \alpha) - g\overline{\gamma}$. This is a displaced thermal state. Explicit calculation using $g = 1$ results in an output state of mean α and 3 units of shot noise, which is identical to that given in hte Heisenberg picture. Note that the gain differs from the Heisenberg picture by a factor of $\sqrt{2}$. This is because the 50/50 beamsplitter attenuation has been absorbed into the measurement, and therefore a projection by $\langle\gamma|$ actually corresponds to a measurement outcome of $\left|\gamma/\sqrt{2}\right\rangle$. This is thus only a matter of notation, and the physical processes which the equations in the two pictures describe are completely identical.

5.3.3 Gaussian Picture

The Gaussian formalism is a simplification of the Heisenberg picture, by including the addional assumption that all states are Gaussian. In such a picture, quantum states can be described exactly by **means** and **covariances**. It is therefore very useful in post-selection schemes, since the equations of conditional probability simplify greatly for Gaussian states.

In the Gaussian picture, we wish to know the mean and covariance at each phase of the teleportation protocol. For simplicity we may consider x only, and the calculations for p would proceed along the same lines. For the x quadrature, we are interested in the **measured mode** x_u, and the **transmitted mode** x_B. Prior to the feedforward, the statistics are

$$\begin{aligned}
\langle x_u \rangle &= x_{in}/\sqrt{2} \\
\langle x_B \rangle &= 0 \\
c &= \begin{bmatrix} (1+\cosh(2r))/\sqrt{2} & -\sinh(2r)/\sqrt{2} \\ -\sinh(2r)/\sqrt{2} & \cosh(2r) \end{bmatrix}
\end{aligned}$$

where c denotes the covariance matrix between x_u and x_B.

After feedforward, we can express the teleporter output as $x_{tel} = x_B + gx_u$, where g denotes an electronic gain. Mean optimisation therefore requires

$$\langle x_B \rangle + g\langle x_u \rangle = x_{in}$$

which leads to $g = \sqrt{2}$ as expected. With this value for the electronic gain g, we may calculate the output variance to be

$$\langle \Delta x_{tel}^2 \rangle = c_{22} + g^2 c_{11} + g c_{21} c_{12} \tag{5.11}$$

and one may plug in values for the covariance matrix elements c_{ij} for an explicit expression of the output variance. Note that the diagonal terms are positive while the off-diagonal terms are negative, which suggests that the entanglement correlations allow the feedforwarding to cancel the noise in the entangled beams.

As one may observe, calculations in this picture is much easier and straightforward, with the drawback that it only applies to Gaussian states. This is sufficient for our purposes, as the post-selection schemes we consider only work for Gaussian inputs.

5.4 Characterisation and Properties

5.4.1 Fidelity

The most obvious criterion for a good teleporter is how well it reproduces the input state. Following the rule of the quantum mechanics community, the figure of merit is the **fidelity**, defined by [5]

$$\mathcal{F} = \langle \psi_{in} | \, \hat{\rho}_{tel} \, | \psi_{in} \rangle$$

where $\hat{\rho}$ denotes the output state which may be a mixed quantum state. Assuming that the input state is coherent, one may use the overlap formula for the Wigner functions to derive an explicit experession for the fidelity

$$\mathcal{F} = \frac{\exp\left(-(1-g)^2 \left(\frac{x_{in}^2}{2(1+\langle \Delta x_{out}^2 \rangle)} + \frac{p_{in}^2}{2(1+\langle \Delta p_{out}^2 \rangle)}\right)\right)}{2\sqrt{(1+\langle \Delta x_{out}^2 \rangle)(1+\langle \Delta p_{out}^2 \rangle)}} \tag{5.12}$$

If the output mean differs from the input, the fidelity is reduced exponentially as the amount of overlap in phase space between the two states decreases. This is captured by the numerator. There is also excess noise introduced by the teleporter originating from imperfect entanglement, which can be described by the denominator.

In the case of unity gain where the electronic gain controls the output mean to be equal to the input mean, the exponential decrease of the fidelity disappears and one obtains

$$\mathcal{F} = \frac{1}{2\sqrt{(1+\langle \Delta x_{out}^2 \rangle)(1+\langle \Delta p_{out}^2 \rangle)}} \tag{5.13}$$

5.4.2 Noise to Gain

A useful pictorial representation of the teleporter is the **noise-to-gain**. One can plot the output variance as a function of the electronic gain (fig.5.4). This figure illustrates the characteristics of a non-ideal teleporter, where the adopted squeezing is pure but finite.

At the mean optimised point, the output state is mean optimised but suffers from excess noise. On the other hand, at the minimal variance point one can achieve the shot noise limit at the cost of attenuation in the mean.

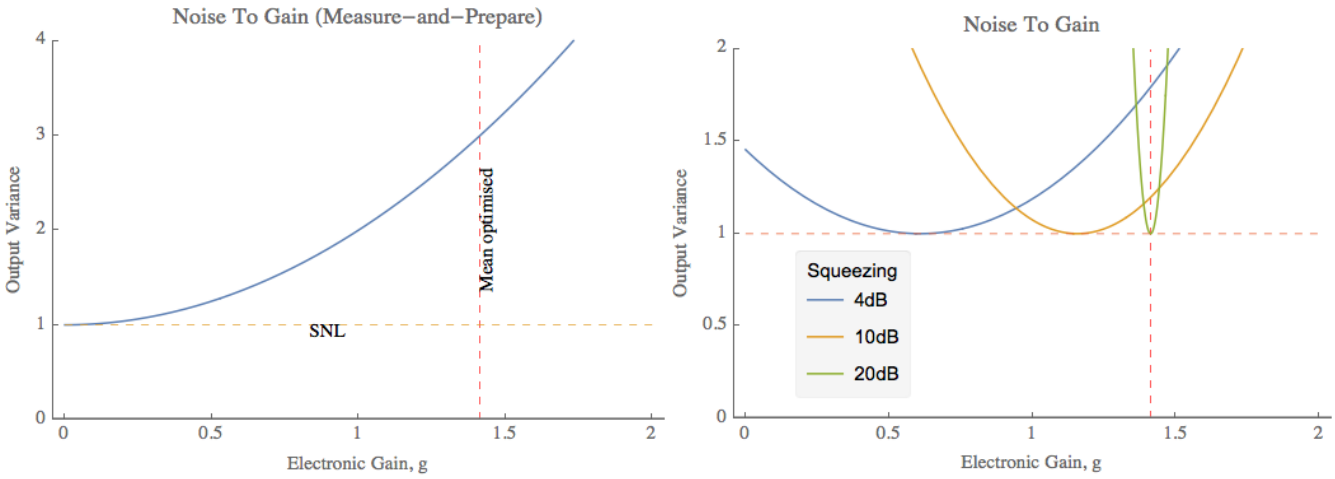

Figure 5.4: Left: no entanglement. Right: increasing entanglement.

To summarise in one sentence: **more feedforwarding is needed to reproduce the input field amplitude than to cancel the EPR noise.** Thus one can either choose to overshoot at the cost of excess noise, or to fall short and comply with an attenuation in the field amplitude.

In the limit $\chi \to 0$ as the entanglement vanishes, the noise-to-gain reduces to that for **measure-and-prepare**.[11] One can observe in fig. 5.4 that the variance is monotonically increasing with respect to the electronic gain, since there are no correlations and therefore the feedforward will simply increase the noise with increased electronic gain. Another feature of this operation regime is that the lowest noise level accessible is two units above the shot noise level. This is the unavoidable noise penalty one must pay in the measure-and-prepare scheme due to the quantum shot noise.

On the other hand, in the regime of strong entanglement the noise -to-gain becomes

One may observe that the overshooting is less; the point of minimal variance has been shifted towards the mean optimised point due to the improving correlations, and coincide in the limit $\chi \to 1$. In such a limit, the entanglement becomes perfect and the teleporter can reproduce the input state with unit fidelity.

5.5 Noiseless Linear Optical Amplification

Due to the unitarity imposed by quantum mechanics, **perfect linear amplification** of the optical bosonic mode is impossible since it alters the commutation relation

$$1 = [\hat{a}, \hat{a}^\dagger] \to [\sqrt{G}\hat{a}, \sqrt{G}\hat{a}^\dagger] = G > 1 \tag{5.14}$$

Physically, the best one can achieve is the **ideal linear amplifier** (ILA) which suffers from

[11] Measure-and-prepare schemes attempt to directly measure quantum states and reconstruct them. These schemes suffer from quantum noise.

invading quantum noise

$$\hat{a} \to \sqrt{G}\hat{a} + \sqrt{G-1}\hat{a}_\nu^\dagger \tag{5.15}$$

with a noise penalty of $|G-1|$ units vacuum noise. With respect to added noise, the ILA represents the optimal amplifier over an entire family of **deterministic linear phase insensitive amplifiers** (DLA). The ILA has been experimentally demonstrated in [16].

In order to go beyond the ILA, one can consider a *probabilistic* regime of amplification [**?**] [12]. By sacrificing the success probability, one may perform **noiseless linear amplification** (NLA) described by the operator $g^{\hat{n}}$ which amplifies a coherent state without introducing additional noise.

$$g^{\hat{n}} |\alpha\rangle = e^{(g^2-1)|\alpha|^2/2} |g\alpha\rangle \tag{5.16}$$

Such an amplifier outperforms the DLA as well as the perfect linear amplification, since it is capable of amplifying the signal without amplifying any noise.

Despite the novel idea, proposals of physical NLA (P-NLA) have turned out to be experimentally challenging [19]. Fortunately, it was found in [12] and demonstrated in [7] that the NLA could be emulated in a *measurement-based* approach. Concretely, an NLA concatenated with dual-homodyne detection has been shown to be equivalent to the dual-homodyne followed by the measurement-based amplifier (MBNLA). The MBNLA is an electronic processing device, consisting of a Gaussian post-selection filter with selection probabilties given by

$$P(\alpha) = \begin{cases} e^{(1-1/g^2)(|\alpha|^2-|\alpha_c|^2)/2} & |\alpha| < \alpha_c \\ 1 & |\alpha| \geq \alpha_c. \end{cases} \tag{5.17}$$

and an electronic attenuation of $1/g_{NLA}$. The cutoff α_c serves to normalise the probabilities.

The NLA cannot be implemented perfectly due to the unboundedness of the operator $g^{\hat{n}}$. In the measurement-based implementation, this glitch translates to the unboundedness of the probabilistic filter. One must truncate the filter. The truncation is described by the cutoff parameter α_c, and defines a trade-off between the success probability and the fidelity; if the α_c is too small with respect to the amplification gain g it will distort the state, and if it is too large then the success probability will be small. Fortunately, a sweet spot can be found where the MBNLA is roughly Gaussian-preserving with a sufficiently high success probability.

Finally, one can combine the NLA and the ILA to form the **hybrid linear amplifier** (HLA). The NLA component allows the HLA to beat the noise limit of ideal linear amplification, while the ILA component shares the burden to achieve a higher success probabilty compared to a stand-alone NLA unit.

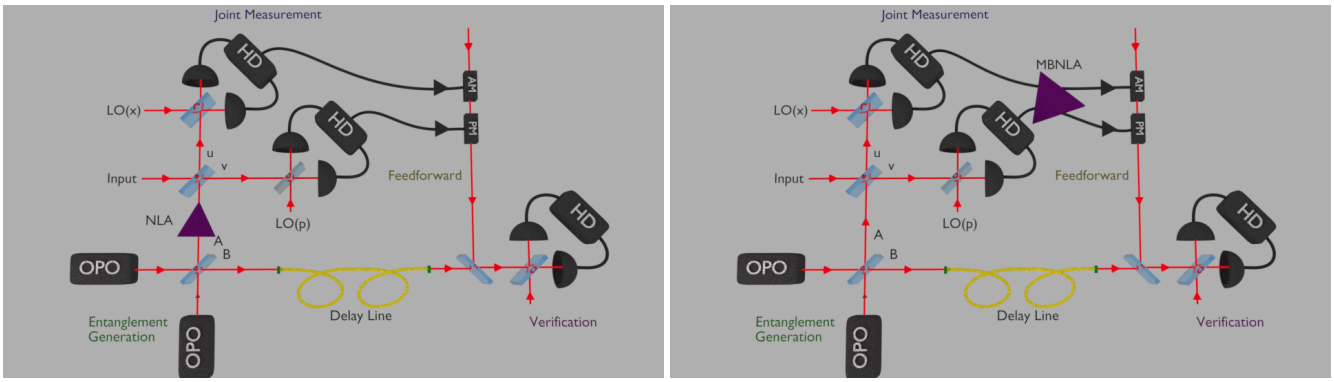

Figure 5.5: Left: directly employing an NLA. Right: using an MBNLA to emulate the NLA.

Dictionary of optical amplifiers:

- **Deterministic linear amplifier** (DLA): A large family based on deterministic amplification. These suffer from greatest excess noise compared with other amplifiers we discussed.
- **Ideal linear amplifier** (ILA): A type of DLA which has the lowest possible excess noise over the family of DLA's.
- **Noiseless linear amplifier** (NLA): Amplification process is non-deterministic (probabilistic), but does not add any noise.
- **Physical noiseless linear amplifier** (P-NLA): Physical implementations of the NLA using optical components to manipulate the state of light directly.
- **Measurement-based noiseless linear amplifier** (MB-NLA): Electronic emulation of the NLA through postselection upon measurement outcomes.
- **Hybrid linear amplifer** (HLA): Concatenation of the NLA and ILA to minimise added noise while maintaining a reasonable success probability. .

5.6 NLA Assisted State Teleporter

5.6.1 Outline

Recently, the noiseless linear amplifier has been applied to perform entanglement distillation and improve the key rate of CV quantum key distribution [7]. More specifically, the adopted amplifier was the measurement-based noiseless linear amplifer (MBNLA) which is much easier to implement compared to its physical counterpart. Using the same idea, we also embed the NLA in the teleportation circuit in hope of improving the entanglement.

The setups for NLA and MBNLA are given in fig. 5.5. It is important to note that they are *not exactly* equivalent; clearly in the first setup the input has not been amplified, while in the

second setup it will have been.

Fortunately, one can show that the two setups behave in more or less the same manner using the Gaussian picture. Therefore **the MBNLA can perform entanglement distillation** to improve the fidelity of the teleporter.

5.6.2 Operation Modes

We wish to operate the NLA to boost the entanglement level of the teleporter. This is not the only possible function of the NLA. The NLA could be employed in the following two ways to increase the fidelity of a teleportation process.

1. Entanglement distilling: increase NLA amplification to increase the entanglement level.
2. Shot noise evading: increase NLA amplification and increase electronic *attenuation* proportionally (i.e. $1/g_{NLA}$), using the idea of a hybrid amplifier.

The first method is the one we will adopt, and will be analysed thoroughly in the next few sections. The second method also increases the fidelity, but is not utilising the entanglement and cannot be considered as a teleporter. More specifically, the noiseless amplification combined with electronic attenuation suppresses the shot noise of the state which improves the measure-and-prepare fidelity.

5.6.3 Quantitative Model

We shall proceed in the Gaussian picture, and consider the x quadrature only. The same calculation holds for the p quadrature.

Before post-selection:

The means and covariance matrix are the same as previous

$$\langle x_u \rangle = x_{in}/\sqrt{2} \tag{5.18}$$

$$\langle x_B \rangle = 0 \tag{5.19}$$

$$c = \begin{bmatrix} (1+\cosh(2r))/\sqrt{2} & -\sinh(2r)/\sqrt{2} \\ -\sinh(2r)/\sqrt{2} & \cosh(2r) \end{bmatrix} \tag{5.20}$$

After post-selection:

Post-selection using filter proportional to

$$\exp\left(\frac{x_u^2}{2}\left(1-\frac{1}{{g_{NLA}}^2}\right)\right)$$

results in modified means and covariance of x_u and x_B which represents the values of the selected subset. We wish to calculate these new quantities. Let us denote the new covariance matrix after the post-selection by $\mathcal{O}$.

By applying the probabilistic filter directly to the Gaussian distribution function, one finds that the mean and variance of x_u after postselection are

$$\tilde{\mu}_u = \frac{\mu_u}{c_{11}\,(1/c_{11} + 1/g^2 - 1)}$$

$$\mathcal{O}_{11} = \frac{1}{1/c_{11} + 1/g^2 - 1}$$

The condition function of x_B given x_u has mean and variance

$$\mu_{B|u} = \mu_B + \frac{c_{21}}{c_{11}}(x_u - \mu_u)$$

$${\sigma_{B|u}}^2 = c_{22} - \frac{c_{21}c_{12}}{c_{11}}$$

It is dependent on the post-selection proceess only through the variable x_u; the functional form is independent of the post-selection process. By comparing the expressions for the conditional mean and variance prior to and after post-selection, we can infer

$$\frac{\mathcal{O}_{21}}{\mathcal{O}_{11}} = \frac{c_{21}}{c_{11}}$$

$$\mathcal{O}_{22} - \frac{\mathcal{O}_{21}\mathcal{O}_{12}}{\mathcal{O}_{11}} = c_{22} - \frac{c_{21}c_{12}}{c_{11}}$$

In terms of the entanglement level $\chi = \tanh r$, we may use equations above to calculate the elements of the covariance matrix $\mathcal{O}$ to be

$$\mathcal{O} = \begin{bmatrix} \frac{g^2}{1-g^2\chi^2} & \frac{\sqrt{2}g^2\chi}{-1+g^2\chi^2} \\ \frac{\sqrt{2}g^2\chi}{-1+g^2\chi^2} & \frac{1}{-1+\frac{2}{1+g^2\chi^2}} \end{bmatrix}$$

Finally, the mean of x_B immediately after post-selection is given by

$$\tilde{\mu}_B = \int dx_u\ \mu_{B|u}\ P(x_u) = \mu_B + \frac{\mathcal{O}_{21}}{\mathcal{O}_{11}}(\tilde{\mu}_u - \mu_u)$$

Feedforward:

With electronic gain ϕ, we obtain

$$x_{tel} = \tilde{x}_B + \phi\ \tilde{x}_u$$

This electronic gain is NOT the same as the g we previously used. It also includes the rescaling in the MBNLA, and is therefore related to g by $\phi = g/g_{NLA}$.

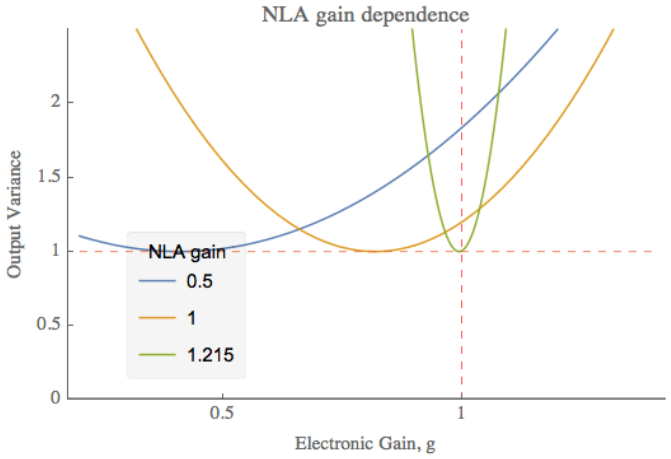

Figure 5.6: Increasing the NLA gain increases the entanglement level.

The output mean and variance are

$$\langle x_{tel} \rangle = \tilde{\mu}_B + \phi \ \tilde{\mu}_u$$

$$\langle \Delta x_{tel}^2 \rangle = \mathcal{O}_{22} + \phi^2 \mathcal{O}_{11} + \phi(\mathcal{O}_{12} + \mathcal{O}_{21})$$

By observing the effective system after post-selection, one finds that the entanglement correlations have increased as χ has been replaced by $g_{NLA}\chi$. Therefore one may define the effective entanglement level after the post-selection as

$$\tilde{\chi} = g_{NLA}\chi \tag{5.21}$$

5.6.4 Performance Analysis

As NLA gain approaches $g_{NLA} = 1/\chi$, the output variance approaches the shot noise limit and the fidelity approaches unity. The effective entanglement becomes perfect in this limit ($\tilde{\chi} \to 1$), and consequently the effective squeezing levels also approach infinity. As an example, given 10dB of squeezing ($\chi = 1.15$) one requires an NLA gain of $g_{NLA} = 1.22$ to achieve unit fidelity. This is within operating conditions for the MBNLA.

The point $g_{NLA} = 1/\chi$ also corresponds to the critical filter. At this value, the post-selection drives the covariance matrix to infinity and therefore any state corresponding to $g_{NLA} > 1/\chi$ is unphysical. More precisely, we mean that there exists no sensible way of normalising states in such a regime.

We can also visualise the effect of the NLA dynamically through the noise-to-gain plot

This is the same effect as increasing the entanglement level in the standard protocol.

5.6.5 Experimental Implementation

Naturally, none of the optical processes can be 100% efficient. To include these inefficiencies, we can simply modify the mean and covariances prior to post-selecting.

Sources of loss and noise:

- Detection efficiency[12]: $\eta = \sqrt{\text{photodiode quantum efficiency} \times \text{mode-matching VIS}^2} \approx 0.987$
- TMSS propagation efficiency: $\xi \approx 0.976$ for both beams, and includes escape efficiency.
- Dark noise clearance: 20dB clearance given by variance $\sigma_d^2 = 1/100$

These are values reported from the best experiments [26], and represents what we should aim to achieve in our experiments in terms of loss suppression.

Inclusion into the teleporter: With an abuse of notation, we shall still use x_B, x_u, and c to denote the corresponding quantities under experimental loss. A rightarrow ($\rightarrow$) indicates what the ideal variables should be replaced by when accounting for loss.

The new quadrature observables are

$$x_B \rightarrow \xi x_B + \sqrt{1-\xi^2}\nu_B$$

$$x_u \rightarrow \frac{\eta}{\sqrt{2}}(x_{in} - \xi x_A - \sqrt{1-\xi^2}\nu_A) + \sqrt{1-\eta^2}\nu_u$$

where ν denotes invading vacuum fluctuations associated with the attenuated mode. Using the same notation as the case without loss, the mean and covariance become

Means:

$$\mu_u \rightarrow \frac{\eta}{\sqrt{2}}x_{in}$$

$$\mu_B \rightarrow 0$$

Covariance:

$$c_{11} \rightarrow \frac{\eta^2}{2}(\sigma_{in}^2 + \xi^2\cosh(2r) + (1-\xi^2)) + (1-\eta^2) + \sigma_d^2$$

$$c_{22} \rightarrow \xi^2\cosh(2r) + (1-\xi^2)$$

$$c_{12} = c_{21} \rightarrow -\frac{\eta\xi^2}{\sqrt{2}}\sinh(2r)$$

With these values established, the rest of the calculation for the teleporter follows exactly the same process.

[12] A reminder that throughout this thesis, all efficiencies are with respect to amplitude. There are other authors who prefer to use power efficiencies.

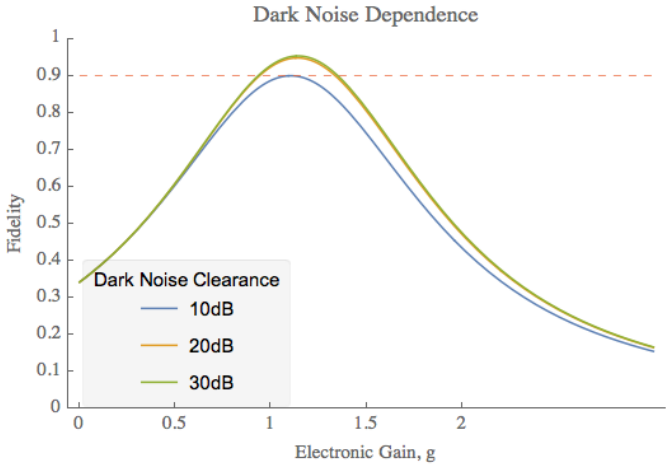

Figure 5.7: Fidelity depends very much on the dark noise clearance.

Results:

For the sake of intuition, we evaluate the output mean and variance for special cases. The full equations are mathematically complicated and do not tell us anything about the physics.

With NLA but without loss ($\xi = \eta = 1, \sigma_d^2 = 0$), the output mean and variance reduce correctly to the equations which does not include the loss. Without NLA but with loss ($g_{NLA} = 1$), and also ignoring dark noise for convenience, equations reduce to standard teleportation protocol with loss, derived in Furusawa *et al.* [**?**] Our equations also correctly reproduces the fidelities of 0.58 and 0.83 obtained in the experiments of [26] and [**?**].

The losses above certainly do not represent all sources in an experiment. But since it fits well with known experimental data, we can safely say that all *dominant* inefficiencies have been taken into account. This model therefore should give a realistic prediction of the performance NLA assisted state teleporter.

- $g_{NLA} = 1$ (without NLA): fidelity = 0.83
- $g_{NLA} = 1.3$ (critical filter): fidelity = 0.95

For the efficiencies listed above, the NLA gain caps at 1.3 (the post-selection filter breaks the state for values larger than that). The maximal fidelity is not unity because the entanglement correlations have been polluted by external noise. While the NLA can fix *weak* entanglement, it cannot fix *impure* entanglement.

From the analysis of the fidelity, one also concludes that the dark noise clearnace can be very important. The fidelity reduces to 0.9 for 10dB dark noise clearance, and shows no further increase beyond 20dB clearance

However, detectors with 10dB clearance are currently much more common than ones with 20dB clearance.

5.6.6 Other Schemes

There have been alternative schemes for embedding an NLA in the teleporter setup, for instance [**?**]. The NLA is deployed for pre-amplification of the input state. Such a scheme suffers from an experimental flaw, as it requires the P-NLA.

5.6.7 Future Possibilites

The MB-NLA is a postselection filter designed to emulate the NLA. This may not be the best or only postselection filter available. For example, redesigning the postselection filter could potentially counter loss, which is a major issue limiting long-distance quantum communication.

5.6.8 Applications

The non-deterministic nature of the NLA-assisted state teleporter implies that online implementations are impractical. However, it could still be useful in offline protocols. For instance, quantum communication requires a crucial component known as the quantum repeater. They are relay stations for long-distance communication, and uses teleportation (in this case also known as entanglement swapping) to establish entangled resources with nearby stations. Provided with sufficient quantum memory, these teleportation processes may be implemented offline in the form of NLA-assisted teleporters.

6 Quantum Gate Teleportation

The quantum gate teleporter is a very useful generalisation of the quantum state teleporter. In contrast to what shows up when one Googles the term "gate teleporter", the quantum gate teleporter refers to a device modifying the state teleporter setup to allow efficient construction of quantum gates. By combining state teleportation and gates, one says that the gate has been *teleported* onto the input state.

6.1 Quantum Gates

To understand the capabilities of gate teleporters, a basic classification of gates will be necessary.

At the highest level of complexity, we consider the **Clifford gates** C_n. They are also known under the names "Gaussian gates" and "linear unitary Bogoliubov transformations" (LUBO). As the names suggest, the Clifford gates correspond to Gaussian preserving transformations generated by displacement operations, phase-shifting, and squeezing operations.

The Clifford gates comprise of the Pauli gates G_n and the symplectic operations $Sp_{2n}(\mathbb{R})$. Physically, Pauli gates correspond to displacement operations. On the other hand, symplectic operations M represents phase shifts and squeezing $M = R(\phi_1)S(r)R(\phi_2)$ via the Bloch-Messiah reduction.

More generally, the Clifford gates decompose as a semidirect product between the symplectic operations and the Pauli gates

$$C_n = Sp_{2n}(\mathbb{R}) \ltimes G_n \tag{6.1}$$

In physical terms, this means that the Clifford gates are formed from products of Pauli gates and symplectic operations, with the special property that the order of any Clifford gate $\hat{C}$ and Pauli gate $\hat{D}$ can be interchanged with only a correction in the Pauli gate. Concretely,

$$\hat{C}\hat{D} = \hat{D}'\hat{C} \tag{6.2}$$

where $\hat{D}'$ is a new Pauli gate. This is relevent to teleportation because feedforwarding is simply a Pauli gate. The property above allows one to freely interchange Clifford gates between either side of the feedforwarding which turns out to be very useful in section 6.5.

6.2 Measurement-Based Squeezing Gate Teleporter

6.2.1 Ideal Protocol

The CV quantum teleportation protocol admits a generalisation to arbitrary measurement bases. It turns out that such a teleporter can perform arbitrary LUBO transformations on the input

quantum state, the most important of which is the squeezing oepration. The power of the embedded state teleporter manifests itself in the *universality* of the gate teleporter, which is to say the squeezing operation may be performed on *arbitrary* input states.

The Heisenberg picture offers a straightforward quantitative description of the squeezing gate teleporter, as given in [24] and summarised below.

Apart from the usual components for state teleportation, this setup has three additional degrees of freedom.

The two important degrees of freedom are angles corresponding to the quadratures q_u and q_v which the dual-homodyne shall be measuring. Concretely,

$$\hat{q}_u = \hat{x}_u \cos\theta_u + \hat{p}_u \sin\theta_u \tag{6.3}$$
$$\hat{q}_v = \hat{x}_v \cos\theta_v + \hat{p}_v \sin\theta_v \tag{6.4}$$
$$\tag{6.5}$$

The other degree of freedom is phase shifting[13] by θ_{in} of the input beam described by

$$\begin{bmatrix} \hat{x}_{in} \\ \hat{p}_{in} \end{bmatrix} \to \begin{bmatrix} \cos\theta_{in} & -\sin\theta_{in} \\ \sin\theta_{in} & \cos\theta_{in} \end{bmatrix} \begin{bmatrix} \hat{x}_{in} \\ \hat{p}_{in} \end{bmatrix} \tag{6.6}$$

By assuming mathematically ideal entanglement:

$$\hat{x}_A - \hat{x}_B = 0 \tag{6.7}$$
$$\hat{p}_A + \hat{p}_B = 0 \tag{6.8}$$

and choosing the feedforward operations to cancel the noise in the entanglement, one can solve directly for the teleported field

$$\begin{bmatrix} \hat{x}_{tel} \\ \hat{p}_{tel} \end{bmatrix} = -\frac{1}{\sin\theta_-} \begin{bmatrix} \sin\theta_+ & \cos\theta_- - \cos\theta_+ \\ \cos\theta_- + \cos\theta_+ & \sin\theta_+ \end{bmatrix} \begin{bmatrix} \cos\theta_{in} & -\sin\theta_{in} \\ \sin\theta_{in} & \cos\theta_{in} \end{bmatrix} \begin{bmatrix} \hat{x}_{in} \\ \hat{p}_{in} \end{bmatrix} \tag{6.9}$$
$$=: M(\theta_+, \theta_-) R(\theta_{in}) \begin{bmatrix} \hat{x}_{in} \\ \hat{p}_{in} \end{bmatrix} \tag{6.10}$$

The transformation above can also be written as

$$M(\theta_+, \theta_-) R(\theta_{in}) = R(-\frac{\theta_+}{2} + \frac{\pi}{4}) S(r(\theta_-)) R(-\frac{\theta_+}{2} - \frac{\pi}{4} - \theta_{in}) \tag{6.11}$$

[13]One should not confuse this with *beamsplitting*. Rotations over two modes are beamsplitting while rotations over quadratures from the same mode is phase shifting.

with the squeezing level given by

$$r(\theta_-) = \operatorname{arctanh} \sin \theta_- \tag{6.12}$$

and the rotation matrices allowing squeezing in arbitrary quadratures. This formula corresponds to a general single mode Clifford transformation[14] up to phase space displacements which can be performed by the modulators. Therefore the measurement-based gate teleporter is capable of teleporting any single mode Clifford gate.

As an example, the measurement angles $\theta_u = \theta_v = 0$ corresponding to measuring the x quadrature on both homodynes along with the phase shift $\theta_{in} = \pi$ results in perfect squeezing in the x quadrature and perfect antisqueezing in the p quadrature. More generally, how much squeezing depends on how much information about the quadrature has been obtained through the measurement. For the case of a teleporter where x and p are measured, no squeezing occurs.

6.2.2 Finite CV Entanglement

The ideal protocol generalises easily in the Gaussian picture to account for finite entanglement. Consider the multivariate Gaussian distribution

$$\mathbf{X} = \begin{bmatrix} x_B \\ p_B \\ q_u \\ q_v \end{bmatrix} \tag{6.13}$$

which is comprised of the quadratures q_u and q_v measured by the homodynes and those transmitted x_B and p_B. The covariance matrix is $c = Cov(\mathbf{X})$ can be computed from first principles $c_{ij} = Cov(X_i, X_j)$.

After feed-forward, the means and variances are given by

$$\begin{aligned} x_{tel} &= x_B + g_{xu} q_u + g_{xv} q_v \\ p_{tel} &= p_B + g_{pu} q_u + g_{pv} q_v \\ \langle \Delta x_{tel}^2 \rangle &= c_{11} + g_{xu}^2 c_{33} + g_{xv}^2 c_{44} + 2(g_{xu} c_{13} + g_{xv} c_{14} + g_{xu} g_{xv} c_{34}) \\ \langle \Delta p_{tel}^2 \rangle &= c_{22} + g_{pu}^2 c_{33} + g_{pv}^2 c_{44} + 2(g_{pu} c_{23} + g_{pv} c_{24} + g_{pu} g_{pv} c_{34}) \end{aligned} \tag{6.14}$$

From the state teleporter, we know that the output mean can be fixed independently of the entanglement level. Therefore the electronic gains can be fixed by comparison of equations 6.14 and equations 6.9. These electronic gains completely determine the variances as well.

The effect of finite entanglement is reduced squeezing and antisqueezing.

[14] See section ref.

6.3 The Squeezing Mechanism

To explain how the gate teleporter performs squeezing, one can consider a toy model where one arm of a two-mode squeezed state is subjected to a homodyne measurement. The information obtained through the measurement is used to squeeze the other beam in the same quadrature which the measurement has been made in.

Concretely, one can calculate the conditional variance of the squeezed quadrature to be $1/\cosh(2r)$. Due to the measurement, all information in its orthogonal quadrature is lost. Thus no conditioning occurs in the orthogonal quadrature of the transmitted beam. The product of the two variances is unity and therefore the squeezing of this state is pure. In particular, this means that the variance $1/\cosh(2r)$ corresponds to maximal squeezing. The Heisenberg uncertainty principle forbids further squeezing.

On the other hand, simultaneous measurements of x and p via heterodyning results in no squeezing; i.e. the conditional state is coherent.

The measurement-based squeezing gate teleporter operates on essentially the same principles as this toy model. Squeezing can be performed on the input state through the dual-homodyne. Measurement of x_u and x_v corresponds to an amplitude squeezing gate; measurement of p_u and p_v corresponds to a phase squeezing gate, and measurement of x_u and p_v corresponds to the state teleporter for which no squeezing occurs.

6.4 NLA-Assisted Gate Teleporter

In this section we discuss application of post-selection to the gate teleporter. In particular, the MBNLA does not function in the same way it did for the state teleporter to the degenerate nature of the homodyning (measuring identical quadratures). A suitable postselection filter shall be constructed, analysed, with further improvements suggested.

6.4.1 The Post-Selection Process

Due to time constraints, we shall consider only one of the simplest case out of many possible generalisations. Fortunately, it will illustrate important properties of the squeezing gate teleporter which holds true even for more complex filters.

The process generalises that for state teleportation. Calculation of input means and covariances proceeds in the same way as section 5.6.3. For convenience, we shall also write the covariance matrix c in blocks of 2×2 matrices

$$c = \begin{bmatrix} \mathbf{\Sigma}_{11} & \mathbf{\Sigma}_{12} \\ \mathbf{\Sigma}_{21} & \mathbf{\Sigma}_{22} \end{bmatrix} \tag{6.15}$$

with each block corresponding to either the measured or the transmitted mode.

According to probability theory, Gaussian preserving postselection filters can be represented by a symmetric matrix $\mathbf{S}$, acting on the measured mode in such a way that

$$\tilde{\mathbf{\Sigma}}_{22}^{-1} = \mathbf{\Sigma}_{22}^{-1} + \mathbf{S} \tag{6.16}$$

The other entries of the new covariance matrix can be calculated using the rules of conditional probability. The feedforward follows in the same way as eq 6.14.

To complete the calculation, all one needs is the postselection matrix $\mathbf{S}$. We shall declare it to be

$$\begin{bmatrix} a & -a \\ -a & a \end{bmatrix} \tag{6.17}$$

with the parameter a given by

$$a = \frac{1}{2}\left(\frac{1}{g^2} - 1\right) \tag{6.18}$$

This filter has a diagonal action on the inputs to the homodyne (x_{in} and x_A), doing nothing to x_{in} while performing noiseless linear amplification on x_A. This filter has been chosen as it has the closest resemblence to the NLA-emulating filter. At the end of this section we will discuss other possible filters within the class of Gaussian preserving postselection processes.

Constrainint output mean to zero for a perfect squeezing gate results in one constraint on each of the pair of electronic gains, leaving one free electronic gain for each quadrature. Without loss of generality, suppose that g_{x_u} and g_{p_u} are free. The final electronic gain can therefore be chosen to minimise the variance and maximise the squeezing. With this, all parameters of the teleporter has been fixed.

6.4.2 Entanglement and Correlations

The noise-to-gain figures are crucial for evaluation of the squeezing gate teleporter. In this section, we provide a way for understanding those figures intuitively, through analysing the correlations.

For EPR beams, a measurement outcome of α from one arm projects the other arm down to a coherent state of amplitude $\chi\overline{\alpha}$. NLA amplifies both quadratures and therefore distills the entanglement.

Tthe single-sided NLA emulating filter in eq.6.17 which we used for the gate *does not* increase the entanglement level of the teleporter. Rather, it increase correlations in x but the correlations in p is lost completely due to the measurement backaction.

6.4.3 Maximal Squeezing

In the gate teleporter, the conditional state of the transmitted beam upon the measurement outcome will define the maximal gate squeezing. Neither postselecting feedforwarding, nor ensenble

averaging will be able to push this bound further. In terms of the state teleporter, this bound of minimal variance corresponds to the SNL. The postselection process is capable of pushing the output state to the shot noise limit, but cannot do any better.

6.4.4 Conclusion

The unfortunate conclusion is that postselection using the filter eq.6.17 does not help.

In this particular case, it is because the dual-homodyne is *degenerate*. Unlike the state teleporter, this results in only one condition on the electronic gains g_{x_u} and g_{x_v}, allowing the remaining free electronic gain to be used for minimising the variance according to the noise-to-gain curve.

More generally, gate squeezing is limited by the conditional variance after the measurement, with the minimal variance obtained when both homodynes are measuring the same quadrature (e.g. x_u and x_v). There cannot exist any postselection scheme which beats this limit.

6.4.5 Future Possibilities

There are multiple ways one can generalise the discussion in this section. For example, for a non-degenerate teleporter, optimisation of the mean requires two degrees of freedom. There are no free electronic gains, and therefore the same filter can be used to decrease the variance. This is similar to how the NLA-emulating filter works for the state teleporter.

The postselection filter could also be generalised. The most general form of a Gaussian preserving filter is given by symmetric matrices, which are more general than eq 6.17

6.5 An Alternative Protocol

There is an alternative version of gate teleportation proposed by Gottesman and Chuang [15][3]. It has came to be known as the **offline** protocol.

The protocol consists of a state teleporter concatenated with a given gate. Of course, such a setup performs the required gate in a trivial way. The interesting observation is that the order of the *feedforward displacement* may be interchanged with the *gate operation*

$$\hat{U}\hat{R} = \hat{U}\hat{R}\hat{U}^\dagger\hat{U} =: \hat{R}'\hat{U} \tag{6.19}$$

In such a way, one obtains an equivalent circuit, with the gate oepration performed on the entanglement resource instead. This protocol is therefore desirable if the gate operation can only be performed non-deterministically. One can wait for it to succeed, before combining it with the input to do the actual online computation.

The kind of gate operations which the offline protocol can teleport correspond to the ones which results in new feedforward operations $\hat{R}'$ that remains simple.

Concretely, if we can only perform coherent displacements (given by the **Pauli gates** $\mathcal{C}_1$), then the kind of gates which could be teleported are the **Clifford gates** $\mathcal{C}_2$ defined by

$$\mathcal{C}_2 = \{\hat{U} \mid \hat{U}\mathcal{C}_1\hat{U}^\dagger \subset \mathcal{C}_1\} \tag{6.20}$$

Of course $\mathcal{C}_2$ will contain all the elements of $\mathcal{C}_1$, and therefore we can construct new gates recursively. Concretely, gates in the class $\mathcal{C}_3 = \{\hat{U} \mid \hat{U}\mathcal{C}_1\hat{U}^\dagger \subset \mathcal{C}_2\}$ can be performed using only feedforward operations in the Clifford group $\mathcal{C}_2$. More generally, one can define

$$\mathcal{C}_k = \{\hat{U} \mid \hat{U}\mathcal{C}_1\hat{U}^\dagger \subset \mathcal{C}_{k-1}\} \tag{6.21}$$

It turns out that such a recursive process can produce *any gate* one desires [15]. Thus in theory, one may utilise the offline protocol to do *universal quantum computation*.

In practice, such a nested sequence of gate teleporters are far too complicated to construct. This is the reason for our decision to focus on only the measurement-based protocol. It is also worth noting that at the first level of recursion which only utilises displacements as feedforward operations, the set of gates each protocol is capable of teleporting coincides.

7 Conclusion

To conclude, we have discovered that the NLA-like filter can boost the entanglement level of the state teleporter but not the gate teleporter due to the degeneracy of the latter. This suggests that one may wish to consider the class of measurement-based protocols with greater resemblence to the state teleporter, in order for postselection to apply. One potential example is the squeezing gate implemented using cluster state computation.

References

[1] Ulrik L. Andersen and Gerd Leuchs. Optical amplification at the quantum limit. *Journal of Modern Optics*, 54(16-17):10–20, 2007.

[2] Hans-A Bachor and Timothy C. Ralph. *A guide to experiments in quantum optics*. Wiley-VCH, 2004.

[3] Stephen D. Bartlett and William J. Munro. Quantum teleportation of optical quantum gates. *Physical Review Letters*, 90(11), 2003.

[4] Eric D. Black. An introduction to pound-drever-hall laser frequency stabilisation. *Am. J. Phys.*, 69(1):79–87, 2001.

[5] Warwick Paul Bowen. *Experiments towards a quantum information network with squeezed light and entanglement*. PhD thesis, Australian National University, 2003.

[6] W.P. Bowen, R. Schnabel, and P.K. Lam. Experimental characterisation of continuous-variable entanglement. *Physical review A*, 69(012304), 2004.

[7] Helen M. Chrzanowski, Nathan Walk, Syed M. Assad, Jiri Janousek, Sara Hosseini, Timothy C. Ralph, Thomas Symul, and Ping Koy Lam. Measurement-based noiseless linear amplification for quantum communication. *Nature Photonics*, 8:333–338, March 2014.

[8] Sheon Chua. *Quantum Enhancement of a 4km Laser Interferometer Gravitational-Wave Detector*. PhD thesis, ANU, 2013.

[9] F.R. Connor. *Modulation*. Edward Arnold, 1982.

[10] R.W.P. Drever, J.L. Hall, Kowalski F.V., J. Hough, G.M. Ford, A.J. Munley, and H. Ward. Laser phase and frequency stabilisation using an optical resonator. *Appl. Phys. B*, 31:97–105, 1983.

[11] Lu-Ming Duan, G. Giedke, J.I. Cirac, and P. Zoller. Inseparability criterion for continuous variable systems. *Physical Review Letters*, 84(12):2722–2725, March 2000.

[12] J. Fiurasek and N. J. Cerf. Gaussian postselection and virtual noiseless amplification in continuous-variable quantum key distribution. *Physical Review*, 86(060302):1–5, 2012.

[13] Akira Furusawa. *Ryoushi kougaku no kiso*. Uchida Rokakuho, 2013.

[14] Akira Furusawa and Peter van Loock. *Quantum Teleportation and Entanglement*. Wiley-VCH, 2011.

[15] Daniel Gottesman and Isaac L. Chuang. Demonstrating the viability of universal quantum computation using teleportation and single-qubit operations. *Letters to Nature*, 402, 1999.

[16] Vincent Josse, Metin Sabuncu, Nicolas J. Cerf, Gerd Leuchs, and Ulrik L. Andersen. Universal optical amplification without nonlinearity. *Physical Review Letters*, 2006.

[17] Ping Koy Lam. *Applications of quantum electro-optic control and squeezed light*. PhD thesis, Australian National University, 1998.

[18] Ulf Leonhardt. *Measuring the quantum state of light*. Cambridge University Press, 1997.

[19] T.C. Ralph and A.P. Lund. Nondeterministic noiseless linear amplification of quantum systems. In Alexander Lvovsky, editor, *Quantum communication, measurement and computing (QCMC): ninth international conference on QCMC*, volume 1110, 2009.

[20] Bahaa E.A. Saleh and Malvin Carl Teich. *Fundamentals of photonics*. John Wiley and Sons, Inc., 1991.

[21] J.H. Shapiro. Quantum optical communication lecture 18.

[22] M. Stefszky. *Generation and Detection of Low-Frequency Squeezing for Gravitational-Wave Detection*. PhD thesis, ANU, 2012.

[23] Jessica Steinlechner, Stefan Ast, Christoph Kruger, Amrit Pal Singh, Tobias Eberle, Vitus Handchen, and Roman Schnabel. Absorption measurements of periodically poled potassium titanyl phosphate (ppktp) at 775 nm and 1550 nm. *Sensors*, 13:565–573, 2013.

[24] Ryuji Ukai, Jun-ichi Yoshikawa, Noriaki Iwata, Peter van Loock, and Akira Furusawa. Universal linear bogoliubov transformations through one-way quantum computation. *Physical review A*, 81(032315), 2010.

[25] Shunhua Wang. *Fabrication and characterisation of periodically-poled KTP and Rb-doped KTP for applications in the visible and UV*. PhD thesis, Royal Institute of Technology Stockholm, 2005.

[26] Hidehiro Yonezawa, Samuel L. Braunstein, and Akira Furusawa. Experimental demonstration of quantum teleportation of broadband squeezing. *Physical Review Letters*, 99(110503), 2007.

[27] Jing Zhang. Einstein-podolsky-rosen sideband entanglement in broadband squeezed light. *Physical review A*, 67(054302), 2003.